January 2018

Scanning Tunneling Microscopy/Spectroscopy Measurements And Density Functional Theory Calculations On Iridium-Modified Silicon Surfaces And Self-Assembled Monolayer Of Organic Molecules On Graphite

Fnu Fatima

SCANNING TUNNELING MICROSCOPY/SPECTROSCOPY MEASUREMENTS AND DENSITY FUNCTIONAL THEORY CALCULATIONS ON IRIDIUM-MODIFIED SILICON SURFACES AND SELF-ASSEMBLED MONOLAYER OF ORGANIC MOLECULES ON GRAPHITE

by

Fatima
Master of Science, University of Dhaka – Bangladesh

A Dissertation

Submitted to the Graduate Faculty

of the

University of North Dakota

in partial fulfillment of the requirements

for the degree of

Doctor of Philosophy

Grand Forks, North Dakota

May
2018

This dissertation, submitted by Fatima in partial fulfillment of the requirements for the Degree of Doctor of Philosophy from the University of North Dakota, has been read by the Faculty Advisory Committee under whom the work has been done and is hereby approved.

Dr. Nuri Oncel

Dr. Graeme Dewar

Dr. Kanishka Marasinghe

Dr. Yen Lee Loh

Dr. Julia Xiaojun Zhao

This dissertation is being submitted by the appointed advisory committee as having met all of the requirements of the School of Graduate Studies at the University of North Dakota and is hereby approved.

Dr. Grant McGimpsey,
Dean of the School of Graduate Studies

April 25, 2018
Date

PERMISSION

Title Scanning Tunneling Microscopy/Spectroscopy Measurements and Density Functional Theory Calculations on Iridium-modified Silicon Surfaces and Self-assembled Monolayer of Organic Molecules on Graphite

Department Physics and Astrophysics

Degree Doctor of Philosophy

In presenting this dissertation in partial fulfillment of the requirements for a graduate degree from the University of North Dakota, I agree that the library of this University shall make it freely available for inspection. I further agree that permission for extensive copying for scholarly purposes may be granted by the professor who supervised my dissertation work or, in his absence, by the chairperson of the department or the dean of the Graduate School. It is understood that any copying or publication or other use of this dissertation or part thereof for financial gain shall not be allowed without my written permission. It is also understood that due recognition shall be given to me and to the University of North Dakota in any scholarly use which may be made of any material in my dissertation.

Fatima
May, 2018

TABLE OF CONTENTS

LIST OF FIGURES……..v

ACKNOWLEDGEMENTS……v

ABSTRACT……v

CHAPTER

I. INTRODUCTION……1

1.1: Iridium-modified Silicon surfaces……2

1.2: Self-assembled monolayers of organic films……3

II. MEASUREMENT METHODS ……5

2.1: Scanning Tunneling Microscopy Theory……6

2.2: X-ray Photoelectron Spectroscopy (XPS)……9

III. DENSITY FUNCTIONAL THEORY……17

3.1: Density Functional Theory (DFT) Calculations……17

3.2: DFT Calculations for Adsorbate on Surface……23

3.3: Conclusion ……27

IV. IRIDIUM ON SILICON (001) SURFACE ……28

4.1: Experimental……28

4.2: Results and Discussion……30

4.3: Conclusion……36

V. OCTANOIC ACID MODIFIED GRAPHITE SURFACE……37

5.1: Experimental……38

5.2: Results and Discussion……40

5.3: Conclusion……43

VI. IRIDIUM ON SILICON (111) SURFACE……45

6.1: Experimental……46

6.2: Results and Discussion……47

6.3: Conclusion……51

VII. 1-DECANETHIOL MODIFIED SILICON (110) SURFACE……52

7.1: Experimental……53

7.2: Results and Discussion……54

7.3: Conclusion……58

VIII. CONCLUSION……59

REFERENCES……61

LIST OF FIGURES

Figure Page

1. UHV System with STM (Right Side) and Sample Preparation Chamber (Left Side)……6

2. An XPS System……9

3. Schematic Diagram of the Photoelectron Spectroscopy Process ……11

4. A Schematic Diagram of Experimental Setup of XPS System……11

5. XPS Spectrum of Ag Before Sputtering……12

6. The Spin-orbit Splitting of the Ir 4f7 Core Level is Indicated by Observation of $4f_{5/2}$ and $4f_{7/2}$ Partner Lines. ……13

7. DFT Model of (a) Top View and (b) Side View of a Four-Layer Slab Model of Octanoic Acid Modified HOPG Surface After Relaxation. ……26

8. (a) A 100 nm × 100 nm STM image of Ir modified Si(001) Surface. ……31

9. (a) and (b) are dI/dV Curves Measured on Ir-silicide and Si(001) Terrace, Respectively……32

10. Proposed Model of Ir-silicide Nanowires on Si(001) Surface……33

11. Calculated Projected DOS Curves of the Proposed Model……34

12. Simulated STM Image for Bias Voltage of (a) -0.658 V and (b) 0.618 V. ……35

13. Proposed Model of Self-assembled Monolayer of Octanoic Acid on HOPG…… 40

14. (a) An 8 nm × 8 nm STM Image of Octanoic Acid on HOPG Surface, V= -1.1 V, I= 0.7 nA……40

15. (a) LDOS Graphs of Octanoic Acid + HOPG (Black Curve) and HOPG (Red Curve) Calculated from Experimental I(V) Curves. ……42

16. (a) Projected DOS of Octanoic Acid Molecules. ……43

17. (a) $20\ \text{nm} \times 20\ \text{nm}$ STM Image of Si(111)- 7×7, $V = -1.312\ V,\ I = 0.688\ nA$.....46

18. (a) Ir-ring cluster on $100\ \text{nm} \times 100\ \text{nm}$ STM Image of Si(111)- 7×7, $V = -1.235\ V, I = 0.414\ nA$ 47

19. LDOS Curves Measured on (a) Si (111) Terrace, and (b) Ir-silicide Islands.....48

20. A Simple Model Showing Surface Free Energies. 48

21. Average Diameter and Average Height of the Islands as a Function of Ir Surface Coverage.....50

22. (a) An 100 nm × 100 nm STM Image of Iridium Modified Si (110) Surface Taken at UHV Conditions, $V = -1.18\ V, I = 0.234\ n$.....53

23. (a) $LDOS$ Graphs of 1-decanethiol + Iridium Modified Si Surfaces Calculated from $I(V)$ Curves Taken on in Between the Islands.....55

24. An XPS Spectrum of 1-decanethiol on Ir-modified Si (110) Surface Where We Can See the Coverage of the Surface.....55

25. Shows (a) Si 2p Peak Measured on 1-decanethiol+ Ir-modified Si Surface. (b) Ir $Ir4f$ Peaks Measured on Ir-modified Si(110) Sample (b) $Ir4f$ Peaks Measured on 1-decanethiol+ Ir-modified Si Surface.....56

26. Shows (a) $C1s$ Peak, and (b) $S2p$ Peaks Measured on 1-decanethiol+ Ir-modified Si (110) Surface.....58

ACKNOWLEDGEMENTS

I would like to express my gratitude to Dr. Nuri Öncel, the chair of my dissertation committee for his continuous support during my doctoral journey. I would like to thank Dr. Kanishka Marasinghe, Dr. Graeme Dewar, Dr. Yen Lee Loh and Dr. Julia Xiaojun Zhao for serving in my dissertation committee. I would also like to thank the rest of the Department of Physics faculty for their support throughout my graduate studies.

I am thankful to my husband Mohammad Gulam Mostofa for his support throughout my doctoral study.

I would like to dedicate this dissertation to my parents, my son Mohammad Mohiuddin, and my daughter Musharat Mubassira.

ABSTRACT

Research was carried out on two different topics, metal induced modifications in various cuts of silicon (Si) surfaces and molecular thin films. But both projects reveal the underlying theme of self-assembly. It is needed to discover functional means to create components for integrated circuits as well as electronic and photonic devices since nature can rely upon self-assembly at the nano-scale.

Scanning Tunneling Microscopy and Spectroscopy (STM/STS) studies were performed to characterize the morphology of thin octanoic acid film on graphite and the outcome of 1-deecanethiol adsorption on the electronic properties of iridium (Ir) modified Si (110) surface. It was established that the octanoic acid and 1-decanethiol molecules can create thin films on graphite surface and Ir-modified Si (110) surface respectively. STM and STS measurements were conducted on Ir-modified Si (001) and Si (111) surfaces. The proposed model of Ir-silicide nanowires shows that Ir atoms are found to sit at the top of the dimer rows of Si(100)-2×1. The Ir-modified Si(111) surface revealed domain formation composed of Ir-ring clusters and metallic Ir-silicide islands formation on top of that domain.

CHAPTER I

INTRODUCTION

Surface effects are becoming more and more important because individual components of electronic devices keep getting smaller.[1] Soon, we will reach to a point where the performance of devices will depend on how atoms and molecules are arranged. Therefore, manipulating and positioning atoms to construct nanoscale devices are fascinating challenges for anybody working in the field of nanotechnology. Prof. Richard Feynman gave a talk on December 29, 1959 at the annual meeting of the American Physical Society at Caltech entitled as 'There's Plenty of Room at the Bottom'[2], he said "The principles of physics, as far as I can see, do not speak against the possibility of maneuvering things atom by atom. It is not an attempt to violate any laws; it is something, in principle, that can be done; but in practice, it has not been done because we are too big." He predicted a revolution in technology if atoms and molecules can be maneuvered as building blocks for construction of functional nano devices in a controlled way. He named this atomic scale fabrication as bottom-up approach that is a complete opposite to top-down approach. Although it has some disadvantages, the top-down approach is commonly used in manufacturing. For example, the sizes of components are limited by the wavelength of light used in lithography[3]. On the other hand, the bottom-up approach uses atoms and small molecules to form functional nanostructures[4]. For the

sign and fabrication of nanodevices for a wide range of potential applications, this method is an alternative to the traditional top-down techniques[5,6].

Although bottom-up approach provides a unique access to quantum world, it is still a very expensive and time consuming process if we want to build every component of integrated circuits for everyday electronics. For that, self-assembly can be used to build nanostructures with novel physical and electronic properties. By using self-assembly, we are not limiting ourselves with the capabilities of current manufacturing technology and we are using well-established thin film growth techniques and basic thermodynamics and kinetics to grow novel nanostructures en mass. Self-assembly based processes, in a way, are our way of trying to mimic the nature. In nature, rather complicated processes with minimum mishaps happen without any human intervention.

In the thesis, we focused on two main self-assembled systems:

i-Iridium modified Si Surfaces

ii-Self-assembled organic thin films.

We studied the physical and electronic properties of these systems experimentally with the help of Scanning Tunneling Microscopy, Low Energy Electron Diffraction, X-ray Photoelectron Spectroscopy. Below, you will find a summary of each project completed.

1.1: Iridium-modified Silicon Surfaces

A variety of stable silicide compounds can be formed by depositing transition metals on Si. Transition-metal-silicon interfaces have widespread application as Ohmic contacts and Schottky-barrier diodes in microelectronic devices. The fabrication of metal-silicon interfaces is commonly used but the chemical trends and the changes in the Schottky-barrier height are still unknown. Therefore, both experimental and theoretical studies are necessary on the chemical composition and the electronic structure of transition-metal-silicon interfaces[7].

We are particularly interested in studying Ir-modified Si surfaces since Ir-silicide has lowest Schottky-barrier for holes and highest Schottky-barrier for electrons which make it suitable for metal semiconductor devices such as metal-oxide-semiconductor field-effect transistor (MOSFET).[8,9] Ir-silicides have three known crystal es, $\mathrm{IrSi}, \mathrm{Ir_3Si_5}$ and $\mathrm{IrSi_3}$. It is possible to grow them selectively in that each silicide phase grows in a specific temperature range and only one silicide phase grows at a given temperature. The samples annealed below $410℃$ show no sign of crystallization. If the annealing temperature is between $410℃$ and $660℃$, then a semi-amorphous Ir_3Si_5 phase forms. $IrSi$ phase forms when the annealing temperature is kept between $660℃$ and $720℃$. Above $720℃$, $IrSi$ phase completely disappears. If the annealing temperature is about $1080℃$, then $IrSi_3$ phase forms. [10,11] One important detail about the crystal phases of iridium silicide is that although $IrSi$ and $IrSi_3$ phases are metallic, Ir_3Si_5 phase is a semiconductor with a band gap of about $1.2 \pm 0.1\ eV$. [12,13]

Another motivation for us to study Ir-modified Si surfaces comes from the fact that various elements ranging from rare-earth metals to transition metals can make novel structures on the flat and vicinal surfaces of Si[14-18]. Those structures are called nanowires for their high aspect ratio.

As a model system, we focused our attention to two different Si surfaces:

i- Ir-modified Si(001): Si(001) surface is still the most commonly used substrate for the fabrication of electronic devices[19-17, 27]. Si(001) surface reconstructs to form rows of dimerized atoms gives which gives its (2×1) reconstruction. We showed that Ir-modified Si(001) surface has nanowires that grow along the direction of dimer rows. The surface is metallic.

ii- Iridium-modified silicon (111) surface: Si (111)-7 × 7 surface is metallic although bulk Si is a semiconductor with a bandgap. Over the years, due to its metallic nature and the famous reconstruction, it has received much attention[28]. Ir-modified Si(111) surface has ring clusters, i.e. Ir atoms surrounded by six Si atoms. The surface is semiconductor with a band gap of about 0.75 eV. Deposition of more Ir leads to the formation of Ir islands.

1.2: Self-assembled Monolayers of Organic Films

For many technologies, it is important to control the properties of surfaces[29]. One method to modify the properties of a given surface is to use the adsorption of organic molecules[30]. Thin films of organic molecules have been applied in different optoelectronic and electronic devices such as electroluminescent devices[31] , sensors[32], diodes[33], and

photovoltaic cells[34] because of their certain physical and chemical properties. It has been shown that self-assembled monolayers can be formed using various types of substrates and molecules. Geometrical structure of the self-assembled layer and the types of the molecules being used influence the properties of the thin film. The morphology of the final layer is governed by the interplay of molecule−substrate and molecule−molecule interactions that can be controlled by varying molecular building blocks, surface structure and chemistry and surface temperature[35]. The self-assembly can be through chemisorption or physisorption depending on the nature of the interaction between the surface and molecules.

We studied two particular organic thin films: Octanoic acid/graphite system and decanethiol/Ir-modified Si(110) system.

i- Octanoic Acid/graphite:

Octanoic acid is a small organic acid (only 8 C atoms) and it is commonly used as an organic solvent. While working on another system we realized that Octanoic acid by itself can form stable thin films on graphite surface. We studied physical and electronic properties of this surface both experimentally and theoretically.

ii- Decanethiol on Ir-modified silicon (110) surface

1-Decanethiol/ Ir-modified Si (110) surface was investigated by STM and X-ray photoelectron spectroscopy (XPS).

CHAPTER II

MEASUREMENT METHODS

In this research, Scanning Tunneling Microscopy (STM) was used as a main experimental tool to collect images of conducting surfaces and its adsorbates with atomic resolution. The experiments performed with two different STMs, Nanosurf EasyScan 2: STM under ambient conditions for Solid-Liquid interface experiments and an Omicron variable temperature STM equipped with Auger Electron Spectroscopy (AES) and low-energy electron diffraction (LEED) for experiments under Ultra-High Vacuum (UHV) conditions as shown in Fig. 1[36]. Along with the STM experiments, X-ray Photoelectron Spectroscopy (XPS) measurements were also done in order to gain complementary information.

The UHV system consists of one rough pump, one turbo pump, and two ion pumps. One of the ion pumps contains titanium sublimation system. In order to reach base pressure of $\sim 2 \times 10^{-10} mbar$ the system is baked for 24 hours at 140°C followed. This chapter includes a brief outline on the working principles of STM and XPS[36].

2.1: Scanning Tunneling Microscopy

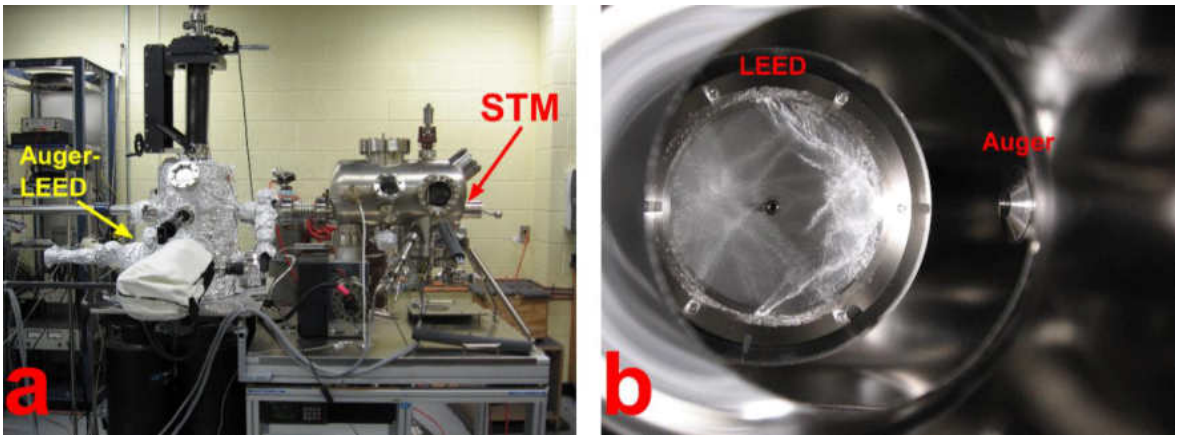

Figure 1. (a) UHV system with STM (right side) and sample preparation chamber (left side). (b) LEED and AES setup, perpendicular to one another.

STM is a powerful tool for studying not only the topography of conducting and semiconducting surface with atomic resolution but also the local electronic properties[37-41] . A sharp metallic tip is used to scan the sample surface and the distance between the sample and the tip is only a few angstroms. After applying a bias voltage to the tip, a small current (in the order of nanoamps) flows between the tip and sample. The current flow can be explained with quantum tunneling. Once a stable tunneling condition is established, the tip starts scanning the sample surface. The movement of the tip can be controlled by a piezoelectric driver in three dimensions (X, Y, or Z) to obtain an image of the surface. A small depression or protrusion can change the tunneling current significantly since tunneling current strongly dependent on the distance between the sample and tip.

Normally, STM operates in two different modes, i.e. constant current mode and constant height mode. In constant current mode, the tip scans the surface while the feedback loop controls the height of the tip in order keep the tunneling current constant. A topographical image of the sample surface with atomic resolution can be obtained by recording the voltages applied to the piezoelectric driver to maintain the constant tunneling current. It is the most commonly used scanning mode since it allows scanning surfaces which are not necessarily atomically flat. Due to the restricted response time of the piezoelectric driver and the feedback loop, the STM has limited scanning speed at this mode.

Tunneling current can be expressed in first-order perturbation theory as

$$I = \frac{2\pi e}{\hbar}\sum_{s,t}\left[f(E_t)\left(1 - f(E_s + eV)\right)\right]\left|M_{s,t}\right|^2 \delta(E_t - E_s) \qquad \ldots\ldots\ldots\ldots\ldots\ldots\ldots (2.1)$$

Where $f(E)$ is the Fermi function, eV is the applied gap voltage, $M_{s,t}$ is the tunneling matrix elements between states ψ_s (surface) with energy E_s and ψ_t (tip) with energy E_t.[33] The equation 2.1 can be more simplified for low temperature and low voltage limits, as most measurements are performed at room temperature or lower and the gap voltage is usually kept within $\pm$ 1 eV of the Fermi level. At low temperatures, the Fermi functions can be considered as step functions near the Fermi energy since almost all the tunneling contributing states are near the Fermi level. At low gap voltages, we can consider the states close to the Fermi energy and the term $\left[f(E_t)\left(1 - f(E_s + eV)\right)\right]$ can be simplified to a delta function. Then we have equation 2.1 as

$$I = \frac{2\pi e^2}{\hbar} V \sum_{s,t}\left|M_{s,t}\right|^2 \delta(E_t - E_F)\,\delta(E_s - E_F) \qquad \ldots\ldots\ldots\ldots\ldots\ldots\ldots\ldots (2.2)$$

Bardeen and Chen showed that at low voltages, the tunneling matrix $M_{s,t}$ can have a continuum limit which relates the measured current to the density of states of the tip and the surface by using an s-orbital wave-function for the tip[42,43] . By considering continuum limit, the tunneling current can be calculated by assigning density of states to both the tip and the sample when the density of states of the surface is dependent of the position and their associated energies. Integrating over all energies contribute to the tunneling, we can write the following equation-

$$I(V,r,z) = \int_0^{eV} \rho_s(r,E)\rho_t(E-eV)T(E,eV,r,z)dE \quad \dots\dots\dots\dots\dots\dots\dots\dots\dots\dots (2.3)$$

Where, $T(E,eV,r,z) = e^{-2z\kappa(E,eV,r)}$, $\kappa(E,eV,r) = \sqrt{\frac{2m}{\hbar^2}\left(\frac{\phi_s(r)+\phi_t}{2} + \frac{eV}{2} - E\right)}$,

ρ is the density of states, κ is the tunneling factor, ϕ_s is the work function of the surface and ϕ_t is the work function of the tip.

$$\frac{dI}{dV} = \rho_s(eV,r)T(eV,eV,r,z) + e\int_0^{eV} \rho_s(E,r)\frac{T(E,eV,r,z)}{dV}dE \quad \dots\dots\dots\dots\dots\dots\dots\dots\dots (2.4)$$

In the equation 2.4, the first term on the right hand side is directly proportional to the surface density of states. The tunneling rate term T and its derivative dT/dV can restrict the resolution of the spectrum since they are exponential functions. By normalizing this derivative (dividing by the total conductance), we can get rid of this difficulty shown.[44] (see eq. 2.5 and 2.6) This is called local density of states (LDOS) which is a well-established method of analyzing electronic properties of the surface.

$$LDOS \equiv \frac{dI/dV}{|I/V|} = \frac{dI}{dV}\left|\frac{V}{I}\right| \quad \ldots\ldots\ldots\ldots\ldots\ldots\ldots\ldots\ldots\ldots\ldots\ldots\ldots\ldots\ldots\ldots (2.5)$$

By normalizing equation(2.4), we have LDOS

$$LDOS \propto \frac{e\rho_s(eV,r) + e\int_0^{eV} \frac{\rho_s(E,r)}{T(eV,eV,r,z)} \frac{dT(E,eV,r,z)}{d(eV)} dE}{\frac{1}{eV}\int_0^{eV} \rho_s(E,r) \frac{T(E,eV,r,z)}{T(eV,eV,r,z)} dE} \quad \ldots\ldots\ldots\ldots\ldots\ldots\ldots\ldots\ldots (2.6)$$

2.2: X-ray Photoelectron Spectroscopy (XPS)

X-ray photoelectron spectroscopy is a widely used surface analysis technique to study elemental compositions, chemical and electronic states of the elements in the sample[45-47]. It needs Ultra-High Vacuum (UHV) conditions.

Figure 2. An XPS system.

Photoelectric effect is the working principle of XPS[48]. An image of XPS system is shown in Figure 2. In this technique a sample surface is irradiating by a beam of X-rays. A core-level electron gains energy from X-ray photon. If gained energy is greater than the

binding energy of electron, the electron will leave the atom. According to the energy conservation rule, the emitted electrons will achieve certain kinetic energy which can be determined by the following equation

$$E_{BE} = h\nu - E_{KE} - \phi \qquad \ldots\ldots\ldots\ldots\ldots\ldots\ldots\ldots\ldots\ldots\ldots\ldots\ldots\ldots\ldots\ldots (2.2)$$

Where $h\nu$ is the total energy of the incoming photon, $E_{BE}$is the binding energy of the electron when it is in initial state, E_{KE} is the kinetic energy of the measured photoelectron and ϕ is the work function of the sample.

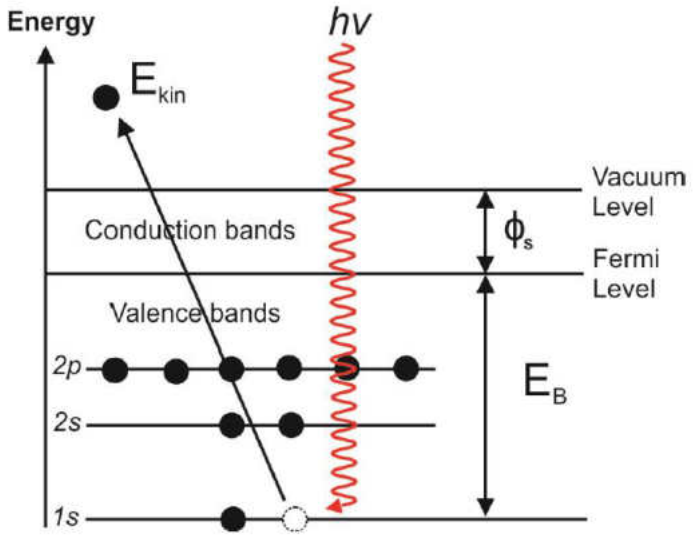

Figure 3. Schematic diagram of the photoelectron spectroscopy process[3].

Figure 4 shows a schematic diagram of the experimental setup of XPS. An XPS system consists of a photon source, a sample which is in an ultra-high vacuum chamber and an electron energy analyzer in order to record the spectra of the photoemission elec-

trons. X-ray tubes are the laboratory sources for XPS, in which x-ray is generated by bombardment of a target with high-energy electrons.

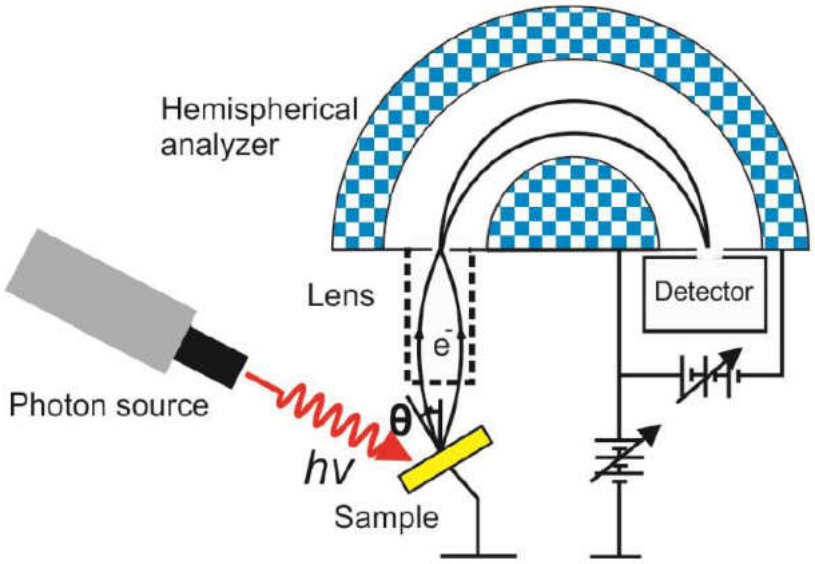

Figure 4. A schematic diagram of experimental setup of XPS system[3].

Mg and Al are two common target materials, for which the emission spectrum is dominated by the unresolved doublet $K_{\alpha 1,2}$ ($2p_{1/2} \rightarrow$ 1s and $2p_{3/2} \rightarrow$1s transitions) at 1253.6eV (Mg $K_{\alpha 1,2}$) and 1486eV (Al $K_{\alpha 1,2}$). For both materials, the linewidth of the $K_{\alpha 1,2}$ doublets amounts to ~ 700-800meV. An XPS spectrum is obtained by measuring the number of emitted photoelectrons as a function of kinetic energy. In the XPS spectrum, the quantitative and qualitative information of the sample elements is obtained on the basis of the analysis of a peak at a particular energy. The cross-section for excitation is different for different electron levels which affects the shape of the spectra. X-ray photons eject electrons not only from the deep core levels but also from the valance band.

The valance band features in the XPS spectrum are very weak due to very low photoelectric cross-section for shallow valence band levels at typical photon energies.

There are some other characteristics such as the continuous background of inelastic secondary electrons and Auger peaks are also shown in Figure 5.

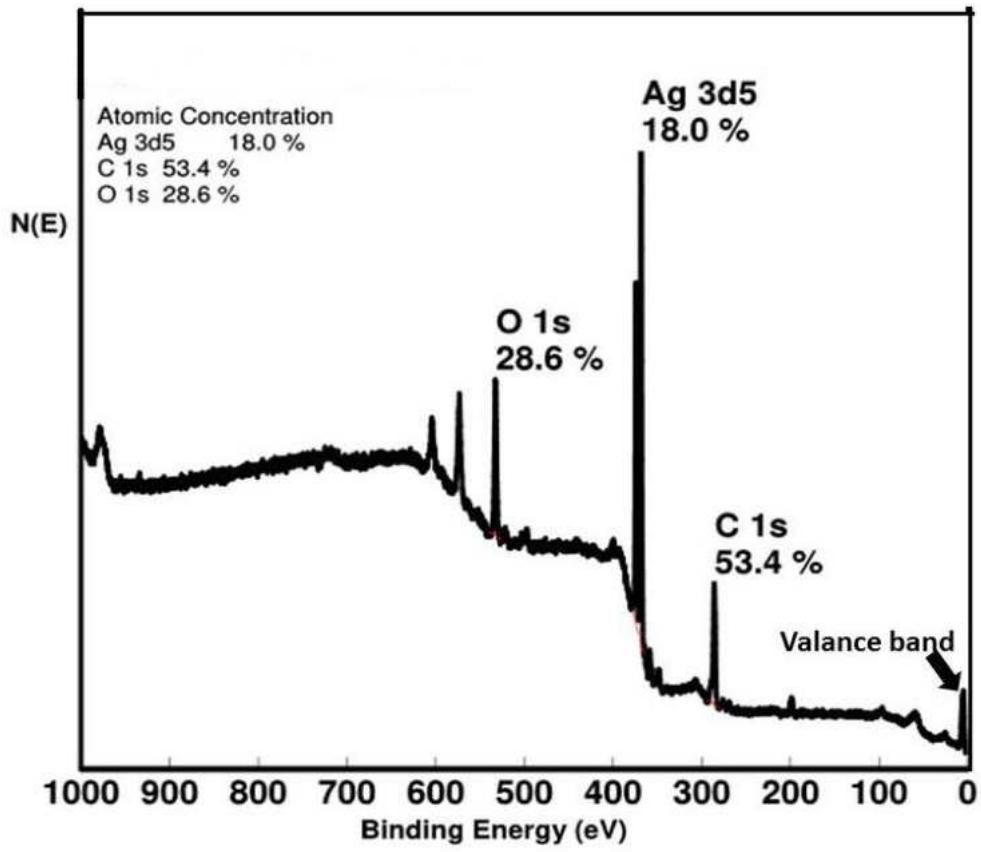

Figure 5. XPS spectrum of Ag before sputtering. The very weak intensity of the valence band features visible at binding energies 0- 5eV.

In XPS spectra, the core levels are visible as sharp peaks and the locations of peaks are defined by the electron binding energies. The XPS spectrum also provides information of the surface composition since the presence of peaks at certain energies is a sign of the

presence of a particular elemental species. By comparing the peak energies on the experimental spectrum with the tabulated binding energies of electrons in elements one can determine which atomic species are present.

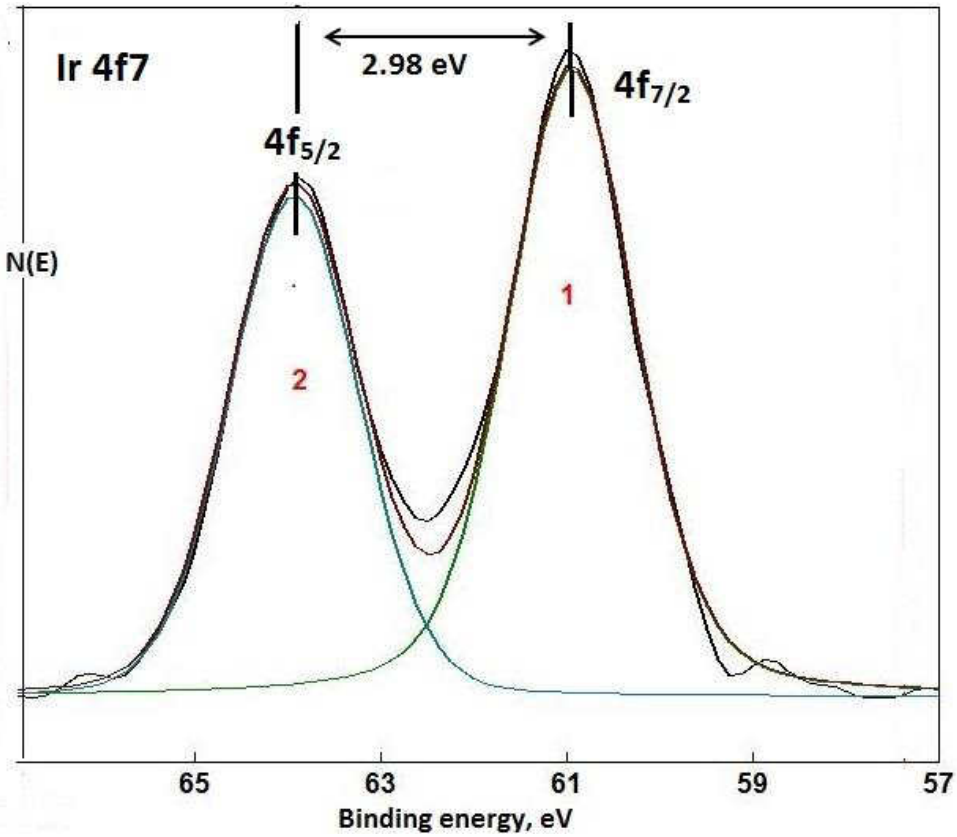

Figure 6. The spin-orbit splitting of the Ir 4f7 core level is indicated by observation of $4f_{5/2}$ and $4f_{7/2}$ partner lines. The splitting of $2.98\ eV$ and the $47_{7/2}$ to $4f_{5/2}$ intensity ratio of 1: 0.75 are atomic properties and practically independent of the chemical environment.

The concentration of the atomic species constituting the surface layer can be estimated from the XPS peak heights. Using XPS one can visualize the fine structure of core levels especially the spin-orbit splitting (Figure 6) with high-energy resolution. For a given element, accurate measurements of the core level peak energies reveal that they vary, de-

pending on its chemical environment and they are called chemical shifts range from 1 to 10eV. The origin of the chemical shifts is as follows.

- At a given level the binding energy of the electron is defined by the interchange between the Coulomb attraction to the nucleus and the screening of this attraction by other electrons in the atom.
- Since the chemical bond formation involves electron transfer, the atomic charge density is changed which results the electron binding energy change.
- The enhanced electron screening associated with the electron transfer to a given atom weakens the electron binding energy i.e., the corresponding peak shifts to shallower binding energies relative to the Fermi level.

Even in the case of adsorbate-free atomically clean surfaces, the environment of the atoms in the surface differs from that in the bulk. This difference appears in the shifts of core levels. Due to the finite penetration depth of x-rays and the limited electron mean free path, the surface components are superposed with bulk components in XPS spectra. In order to increase the surface sensitivity of XPS, usually grazing incidence radiation and collection of photoemission electrons at grazing angles are used. Additionally, the fraction of the signal coming from various depths can be altered for analyzing the depth distribution of a given atomic species by changing the polar angle of the detector[46].

CHAPTER III

DENSITY FUNCTIONAL THEORY

3.1 Density Functional Theory (DFT) Calculations

In many engineering and physical science fields, understanding and controlling the properties of matter at the level of individual atoms and molecules is the key to scientific and technological progress. Density functional theory is a successful technique to find the solutions of Schrödinger equation which describes the quantum behavior of atoms and molecules.

3.1.1 The Many-Body Problem

We are interested in a situation where multiple electrons are interacting with multiple nuclei. The time independent Schrödinger equation in this case is

$$[-\frac{\hbar^2}{2m}\sum_{i=1}^{N}\nabla_i^2+\sum_{i=1}^{N}V(\boldsymbol{r}_i)+\sum_{i=1}^{N}\sum_{j<i}U(\boldsymbol{r}_i,\boldsymbol{r}_j)]\psi=E\,\psi \ldots\ldots\ldots\ldots\ldots\ldots(1)$$

Where, m is the mass of electron. The first term in the bracket is the kinetic energy of each electron, the second term in the bracket is the interaction energy between each electron and the collection of atomic nuclei and the third term is the interaction energy between different electrons. We have chosen ψ as the electronic wave function for the Hamiltonian which is a function of each of the spatial coordinates of each of the N electrons, so $\psi = \psi(\boldsymbol{r}_1,\ldots\ldots\ldots,\boldsymbol{r}_N)$, and E is the ground state energy of the electrons. It

is possible to write ψ as a product of individual electron wave functions, $\psi = \psi_1(\boldsymbol{r})\,\psi_2(\boldsymbol{r}), \ldots\ldots, \psi_N(\boldsymbol{r})$ despite the electron wave function is a function of each of the coordinates of all N electrons. When the wave function is expressed in this way is called Hartree product.

From the point of view of solving the equation, electron-electron interactions term in the Hamiltonian is the most critical one. The Schrödinger equation is a many-body problem. The wave function for any particular set of coordinates cannot be directly observed. The probability that the N electrons are at a particular set of coordinates, $\boldsymbol{r}_1, \ldots\ldots, \boldsymbol{r}_N$ can be measured and it is equal to $\psi^*(\boldsymbol{r}_1, \ldots\ldots, \boldsymbol{r}_N)\,\psi(\boldsymbol{r}_1, \ldots\ldots, \boldsymbol{r}_N)$. The density of electrons at a particular position in space, $n(\boldsymbol{r})$ can be written in terms of the individual electron wave functions as

$$n(\boldsymbol{r}) = 2\sum_i \psi_i^*(\boldsymbol{r})\psi_i(\boldsymbol{r}) \ldots\ldots\ldots\ldots\ldots\ldots (2)$$

The equation (2) consists the factor of 2 since each individual electron wave function can be occupied by two separate electrons and they have different spins. The term inside the summation is the probability that an electron in individual wave function $\psi_i(\boldsymbol{r})$ is located at position $\boldsymbol{r}$.

3.1.2 The Hohenberg- Kohn Theorem

The density functional theory based on two fundamental mathematical theorems proved by Kohn and Hohenberg and it also depends on the derivation of a set of equations by Kohn and Sham. The first theorem is:

"*The ground-state energy from Schrödinger's equation is a unique functional of the electron density*".

According to this theorem, there is a one-to-one mapping between the ground-state electron density and the ground-state wave function. We can state Hohenberg and Kohn's result in another way that the ground-state energy E can be expressed as $E[n(r)]$, where $n(r)$ is the electron density. That's why it is called density functional theory. Even though Hohenberg and Kohn theorem proves that there is a functional of the electron density exists which can be used to solve the Schrödinger equation but the theorem does not say what the functional is. The second Hohenberg-Kohn theorem provides a major characteristic of functional:

"The electron density that minimizes the energy of the overall functional is the true electron density corresponding to the full solution of the Schrödinger equation".

We could vary the electron density until the energy from the functional is minimized if the true functional form were known, in this way we could find the relevant electron density. In practice with approximate forms of the functional this variational principle is used.

According to Hohenberg-Kohn theorem the functional can be written down in terms of the single-electron wave functions, $\psi_i(\boldsymbol{r})$. These wave functions collectively define the electron density, $n(\boldsymbol{r})$. The energy functional can be expressed as

$$E[\{\psi_i\}] = E_{known}[\{\psi_i\}] + E_{XC}[\{\psi_i\}] \dots\dots\dots\dots\dots (3)$$

The known terms consists four terms:

$$E_{known}[\{\psi_i\}] = \frac{h^2}{m}\sum_i \int \psi_i{}^* \nabla^2 \psi_i d^3r + \int V(\boldsymbol{r}) n(\boldsymbol{r}) d^3r + \frac{e^2}{2}\int\int \frac{n(\boldsymbol{r})n(\boldsymbol{r}')}{|\boldsymbol{r}-\boldsymbol{r}'|} d^3r d^3r'$$

$$+ E_{ion} \ldots\ldots\ldots\ldots\ldots\ldots\ldots\ldots\ldots\ldots\ldots\ldots\ldots\ldots\ldots\ldots\ldots (4)$$

The term on the right side are, kinetic energies of electron, the Coulomb interactions between the electrons and the nuclei, the Coulomb interaction between pairs of electrons, and the Coulomb interactions between pairs of nuclei respectively. The other term $E_{XC}[\{\psi_i\}]$ in equation (3), is the exchange-correlation functional and it includes all the quantum mechanical effects that are not included in the “known” terms. The description so far does not guarantee that finding minimum energy solutions of the total energy functional is easier than solving the Schrödinger equation for wave function.

3.1.3 The Self-Consistent Kohn-Sham Equations

Kohn and Sham first showed that the way of finding the right electron density involves a set of equations in which each equation associated with only one electron. The Kohn –Sham equations is

$$\left[\frac{h^2}{2m}\nabla^2 + V(\boldsymbol{r}) + V_H(\boldsymbol{r}) + V_{XC}(\boldsymbol{r})\right]\psi_i(\boldsymbol{r}) = \varepsilon_i \psi_i(\boldsymbol{r}) \ldots\ldots\ldots\ldots\ldots\ldots\ldots\ldots (5)$$

There are three potentials on the right sides, V, V_H, and V_{XC}. The first potential defines the interaction between an electron and the collection of atomic nuclei and it is included to the full Schrödinger equation (Eq.(1)) and the total energy functional (Eq.(4)). The second one is the Hartree potential which is defined by

$$V_H(\boldsymbol{r}) = e^2 \int \frac{n(\boldsymbol{r}')}{|\boldsymbol{r}-\boldsymbol{r}'|} d^3r' \ldots\ldots\ldots\ldots\ldots\ldots\ldots\ldots\ldots\ldots\ldots\ldots\ldots\ldots (6)$$

Since the electron we are describing in the Kohn-Sham equation is part of the electron density, the Hartree potential includes a Coulomb interaction between the electron and itself. The correction for the self-interaction contains in the final potential in the Kohn-Sham equations V_{XC} which defines exchange and correlation contributions to the single-electron equations. The exchange and correlation V_{XC} is functional derivative of the exchange-correlation energy:

$$V_{XC}(\boldsymbol{r}) = \frac{\delta E_{XC}(\boldsymbol{r})}{\delta n(\boldsymbol{r})} \dots\dots\dots\dots\dots\dots\dots\dots\dots\dots\dots\dots\dots\dots\dots (7)$$

In order to solve the Kohn-Sham equations, it is needed to know Hartree potential. To determine the Hartree potential, we need to know the electron density. To define the electron density, we have to know the single-electron wave functions, and to know these wave functions we must have to solve Kohn-Sham equations. The following algorithm is used in an iterative way to break this circle:

1. Define a trial electron density, $n(\boldsymbol{r})$.
2. Find the single-particle wave functions $\psi_i(\boldsymbol{r})$ by solving Kohn-Sham equations using the trial electron density from step 1.
3. From step 2 get the electron density defined by the Kohn-Sham single-particle wave functions, $n_{KS}(\boldsymbol{r}) = 2\sum_i \psi_i^*(\boldsymbol{r})\psi_i(\boldsymbol{r})$.
4. Compare the trial electron density, $n(\boldsymbol{r})$ with calculated electron density, $n_{KS}(\boldsymbol{r})$. If they are similar then it is the ground state electron density and can be used to evaluate total energy. If the two densities are not same, then the trial density should be updated. After doing this the process resume from step 2.

3.1.4 Exchange-Correlation Functional

The existence of exchange-correlation functional is guaranteed by the Hohenberg-Kohn theorem and exact form is unknown. This functional can be derived exactly in case of uniform electron gas where the electron density is constant at all points in space, that is, $n(\boldsymbol{r})$ = constant. The practical way to use the Kohn-Sham equations is given by the uniform electron gas. The exchange-correlation potential is set at each position as the known exchange-correlation potential from the uniform electron gas at the density observed at that position:

$$V_{XC}(\boldsymbol{r}) = V_{XC}^{electron\ gas}[n(\boldsymbol{r})] \ldots\ldots\ldots\ldots\ldots\ldots\ldots\ldots\ldots\ldots\ldots\ldots (7)$$

To define the approximate exchange-correlation functional this approximation only uses the local density that's why it is called the local density approximation (LDA). Although this approximation gives us a way to completely define the Kohn-Sham equations, the result from these equations do not exactly solve the true Schrödinger equation since the true exchange-correlation functional is not using. After the LDA the best known class of functional is generalized gradient approximation (GGA) which uses information about the local electron density and the local gradient in the electron density.

There are a large number of GGA functionals since there are many ways in which information from the gradient of the electron density can be included in a GGA functional. In the calculations involving solids there are two most widely used functionals are Perdew-Wang functional (PW91) and the Perdew-Burke-Ernzerhof functional (PBE). For

any particular configuration of atoms different functionals will give different results, so it is necessary to mention which functional was used for any particular calculations.

3.2 DFT Calculations for Adsorbate on Surfaces

In many successful projects, DFT and surface science have been teammates. Ultra-high-vacuum surface science experiments such as scanning tunneling microscopy, temperature-programmed desorption, X-ray diffraction, and X-ray photoelectron spectroscopy along with DFT has been used to determine the surface structure of metals, metal oxides, nanoparticles, carbides, and sulfides.

3.2.1 Periodic Boundary Conditions and k points

We want to apply DFT calculations to periodic arrangements of atoms in space. A cell which is repeated periodically in space by lattice vectors $\boldsymbol{a}_1$, $\boldsymbol{a}_2$, and $\boldsymbol{a}_3$ is called the supercell. The solution of Schrödinger equation for this periodic system is Bloch's theorem:

$$\phi_k(\boldsymbol{r}) = \exp(i\boldsymbol{k}.\boldsymbol{r})\, u_k(\boldsymbol{r}) \dots\dots\dots\dots\dots\dots\dots\dots\dots\dots (8)$$

Where $u_k(\boldsymbol{r})$ is periodic in space i. e., $u_k(\boldsymbol{r} + n_1\boldsymbol{a}_1 + n_2\boldsymbol{a}_2 + n_3\boldsymbol{a}_3) = u_k(\boldsymbol{r})$ for any integers n_1, n_2, and n_3. Since the functions $\exp(i\boldsymbol{k}.\boldsymbol{r})$ are plane waves, calculations based on this idea are known as plane-wave calculations. In DFT calaculations, it is necessary to specify how many k points are to be used in each direction in reciprocal space. Same number of k points is used in each direction for calculations using supercells with same length along each lattice vector and the same length along each reciprocal lattice vector.

In each direction if Mk points are used, the calculations are label as using $M \times M \times Mk$ points[49].

3.2.2 Energy Cutoffs and Pseudopotentials

Whenever a DFT calculation is performed, the cutoff energy, E_{cut} must be defined. It is easier to define this parameter compare to k points since most packages will apply sensible default settings if no other information is provided by the user. It is not wise to use default value of cutoff energy when a cutoff energy is assigned for each element and the largest cutoff energy for any of the atoms in the supercell is assigned as the overall cutoff energy. The large energy cutoffs is used for plane waves that oscillate on short length scales in real space but the tightly bound core electrons in atoms are associated with the wave functions with this kind of oscillation. The core electrons are not significant in defining physical end electronic properties of materials; less tightly bound valence electrons dominate this property. To reduce the computational burden of core electrons pseudopotentials are used. Actually, the electron density from a chosen set of core electrons with a smoothed density chosen to match different physical and mathematical properties of the true ion core is replaced by pseudopotential. In all subsequent calculations the properties of the core electrons are constant in this approximate form.

3.2.3 Surface Relaxation

The atoms or molecules are placed on top of multilayer slab. The distance between two adjacent layers is constant in a bulk metal. But the spacing between the layers of the material is not same near the surface. The spacing between layers near the surface

might be different from those in the bulk since the coordination of atoms in the surface is reduced compared with those in the bulk. This phenomenon is known as surface relaxation and our goal of initial calculations with surface is to characterize this relaxation.

Relaxed surface has lower energy compare to original surface. By performing energy minimizations as a function of the positions of the atoms in the supercell we can find the geometry of the relaxed surface[1].

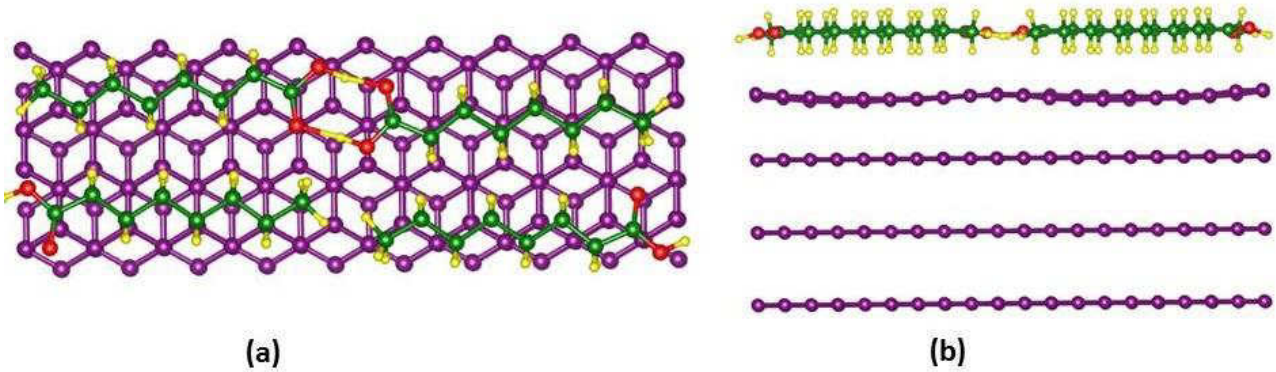

Figure 7. DFT Model of (a) top view and (b) side view of a four-layer slab model of octanoic acid modified HOPG surface after relaxation. Carbon, oxygen and hydrogen atoms of octanoic acid molecules are in green, red and yellow, respectively.

We will look at situations where atoms or molecules are adsorbed on surfaces and chemical bonds form between the atom or molecule and the surface. We will calculate surface energy, density of state (DOS), partial density of state (PDOS), and STM image.

CHAPTER IV

IRIDIUM ON SILICON (001) SURFACE

Building nanostructures with unique electronic properties on flat and/or vicinal Si (silicon) and Ge (germanium) substrates have been the goal of many researchers[50-56]. Since these substrates are mainly used in semiconductor industry, they can provide a smooth transition from a prototype in a research lab to a consumer product. Some of these structures have high aspect ratios therefore, they are called nanowires. Nanowires may exhibit interesting phenomena such as quantum confinement[57,58], Peierls instability [59-61], Luttinger liquid [62]. They can be made up of various elements ranging from Bismuth[63] and rare-earth metals [64-66] to transition metals[67,68]. Among those, transition metal nanowires have a special place because of the fact that they don't react with air to form insulating oxide layers. Ir (iridium) has already been shown to form nanowires on Ge (001), Si (001) and Si (110) surfaces [69-71]. Here, we report Scanning Tunneling Microscopy/Spectroscopy (STM/STS) data to reveal electronic properties of Ir-silicide nanowires.

4.1: Experiments

We purchased Ir (99.9 %) wire from Goodfellow. We used a p-type and B-doped Si (001) substrate. The samples were mounted on molybdenum holders and contact of the samples to any other metal during preparation and experiment were carefully avoided.

The ultra-high vacuum (UHV) system is equipped with Omicron variable temperature Scanning Tunneling Microscopy (STM) and LK technologies RVL2000 Low energy electron diffraction (LEED)-Auger spectrometer system. The base pressure of the system was kept below $5 \times 10^{-10}\ mbar$. Before introducing Si(001) samples in the UHV chamber, samples were dipped in isopropanol and dried with N_2 gas. Si(001) samples were degassed in the vacuum for at least two days prior to flash-annealing cycles at 1250 ℃. The quality of the clean Si(001) samples was checked and confirmed both with LEED and STM before depositing Ir. 0.25 monolayer of Ir was deposited over the clean Si(001) surfaces from a direct current heated Ir wire. After deposition at room temperature, the sample was annealed at $700℃$. The sample temperature was measured with a pyrometer.

Theory:

For theoretical calculations we collaborated with Ismail Can Oguz ,Deniz Çakır, and Oguz Gulseren . All calculations were performed within plane-wave pseudopotential method based on density functional theory as implemented in the Vienna Ab-initio Simulation package (VASP)[72].The ions were described by employing PAW pseudopotential for atomic core region[73]. The generalized gradient approximation was used for the exchange-correlation functional. Plane wave basis set was used for the expansion of the Kohn-Sham orbitals. After the extensive test calculations for the total energy convergence, the kinetic energy cut-off for plane wave expansion was set to 400 eV. The Brillouin zone (BZ) of the silicon surface is sampled with a k-mesh of 10×10×1 within Monkhorst-Pack scheme[74]. A vacuum region of 15 Å is introduced in order to prevent

spurious interaction between the periodic slabs. In order to minimize the interaction of silicon surfaces at the bottom and top of the slab structure, the number of layers were determined by observing relaxation shift of the first layer atom positions. Test calculations revealed that nine silicon layers were sufficient to describe Si(001) surface accurately. Four bottom layers were fixed at their corresponding bulk atomic positions in the calculations. Moreover, hydrogen atoms were attached to all silicon atoms at the bottom layer in order to saturate the dangling bonds. Thus, a system was obtained by resembling the Si-bulk crystal. Except the atoms in the four lower layers, all the other atoms were allowed to relax and reconstruct.

4.2: Results and Discussions

The LEED and STM measurements showed that, if annealed at 700 °C, Ir-modified Si(001) surface turned into relatively small, irregular-shaped Ir-silicide terraces that exhibit a $p(2 \times 2)$ LEED pattern. If the sample was annealed above 800 °C, these terraces disappeared and Si(001) surface started to come back. The nanowires on the terraces stretch along [110] directions similar to dimer rows of a pristine Si(001) surface[53,75].This indicates that the morphology of Si(001) surface directly influences the structure of these nanowires. The surface has Ir-rich terraces surrounded by Si(001) terraces with high density of vacancy line defects. (See Figure 8a) Figure 8b and 8c shows high resolution STM images of Ir-rich terraces.

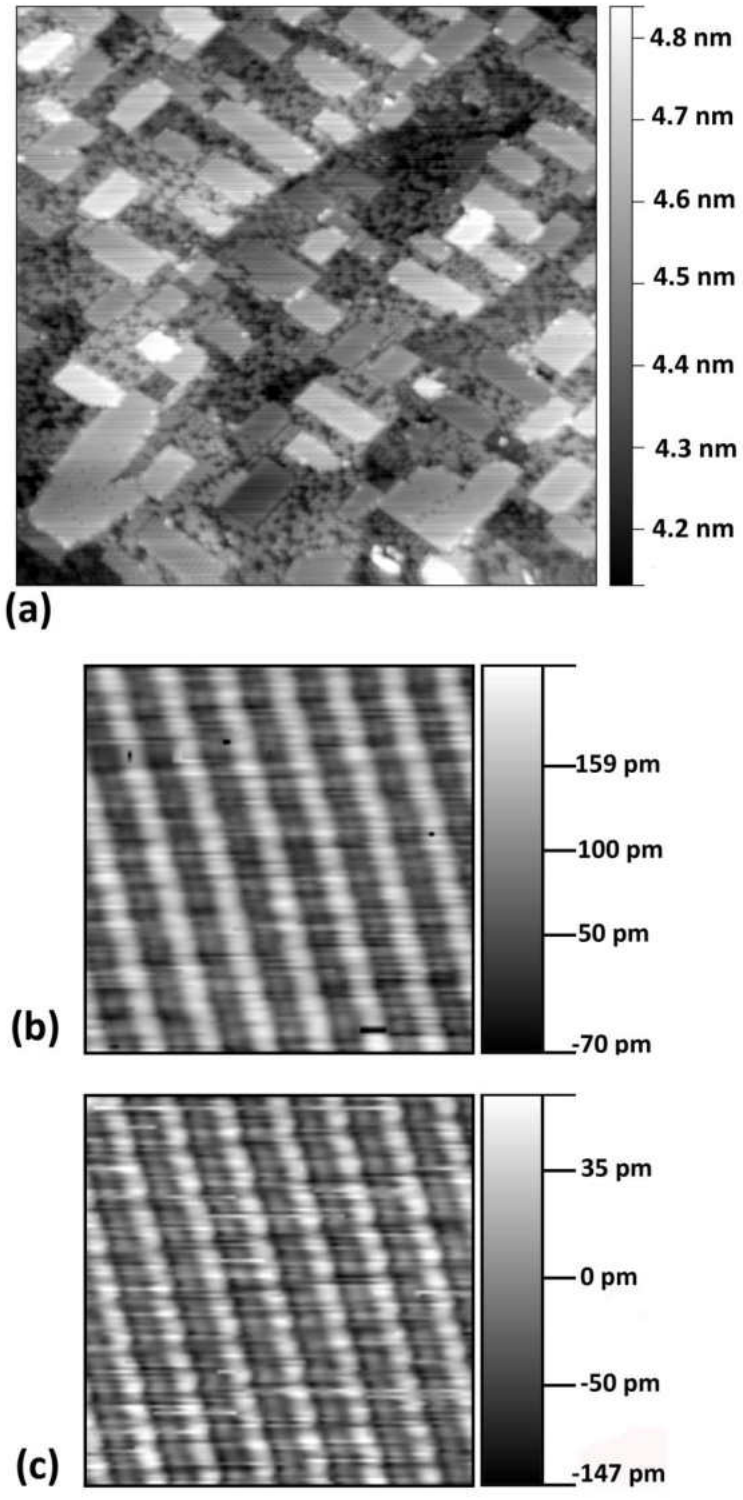

Figure 8. (a) A 100 nm × 100 nm STM image of Ir modified Si(001) surface. The sample bias and the tunneling current are -1.74 V and 0.43 nA, respectively. (b) and (c) are 6 nm × 6 nm STM image of Ir-silicide nanowires. The images are from the same region recorded at the same time during forward and backward scanning. The scanning voltages are 0.619 V and -0.658 V, respectively. The tunneling current is 0.49 nA.

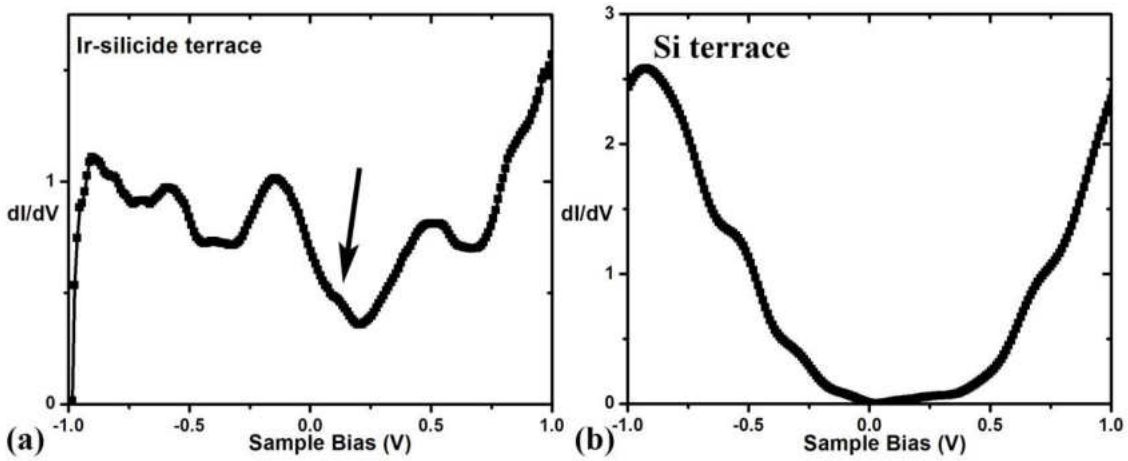

Figure 9. (a) and (b) are dI/dV curves measured on Ir-silicide and Si(001) terrace, respectively.

In order to study electronic properties of the nanowires, we performed I-V measurements at 77 K (see Figure 9a). We calculated dI/dV curves numerically from the measured I-V curves. We didn't see any difference between the dI/dV curves measured on the nanowires and in the trough between the nanowires. dI/dV curves measured on the nanowires have nonzero conductance around the Fermi level indicating that the nanowires are metallic. There are three well-resolved peaks located at about -0.57 V, -0.15 V and 0.50 V. On the other hand, the dI/dV curves measured on the Si(001) surface by the Ir-silicide terraces have a band gap of about 0.5 eV which is in line with the previously reported data on Si(001)[76].

Considering both the calculations on the adsorption of a single Ir atom and measured STM images, we came up with a model of Ir-silicide nanowires (See Figure 10).

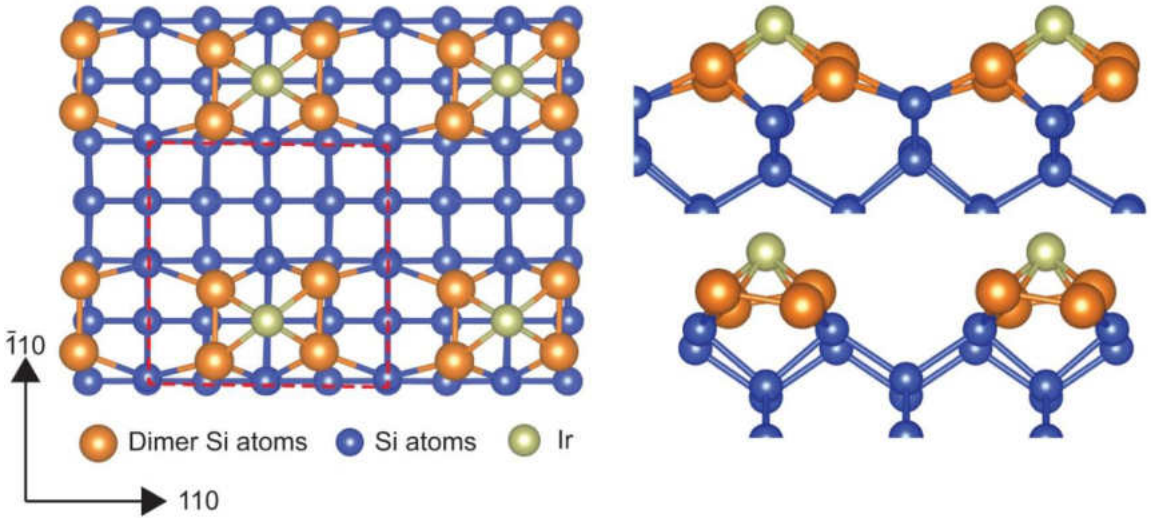

Figure 10. Proposed model of Ir-silicide nanowires on Si(001) surface. Left (right) is a top (side) view of the proposed surface. Red dashed lines enclose a 2×2 surface cell.

We compared measured dI/dV curves with calculated DOS curves for the proposed model (See Figure 10). The model predicts that the surface is metallic and there are three well-resolved peaks around the Fermi level. Similarly, the fluorite-type $IrSi_2$ also exhibits metallic behavior[77]. A quick comparison reveals that the experimental dI/dV curves and the calculated DOS curves show remarkable similarities. Both have states located at about -0.55 eV, -0.13 eV and 0.46 eV indicating that the proposed model accurately reproduces the measured electronic properties of the system. A well-defined peak right above the Fermi level in the calculated DOS graph is vaguely visible in the experimental dI/dV curves (indicated by an arrow). We attribute the vagueness of this peak to the broadening of the STS peaks at finite temperature. In order to find out the origins of the observed states, projected DOS curves for the dimer atoms and Ir atom of the surface have been calculated (See Figure 11). Since the Ir atom sits on the top dimer row, its contribution to the DOS, especially, below the Fermi level is significant. The state at 0.46 eV

has almost equal contributions from both Si dimers and Ir atom. The calculated DOS points out a strong interaction between Si and Ir atoms and hybridization between Si *p* states and Ir *d* states. In order to correlate the proposed model with the measured STM images, STM images have also been calculated for bias voltages of -0.658 V and +0.618 V, see Figure 12.

Unlike experimental data shown in Figure 8b and 8c, the calculated STM images of

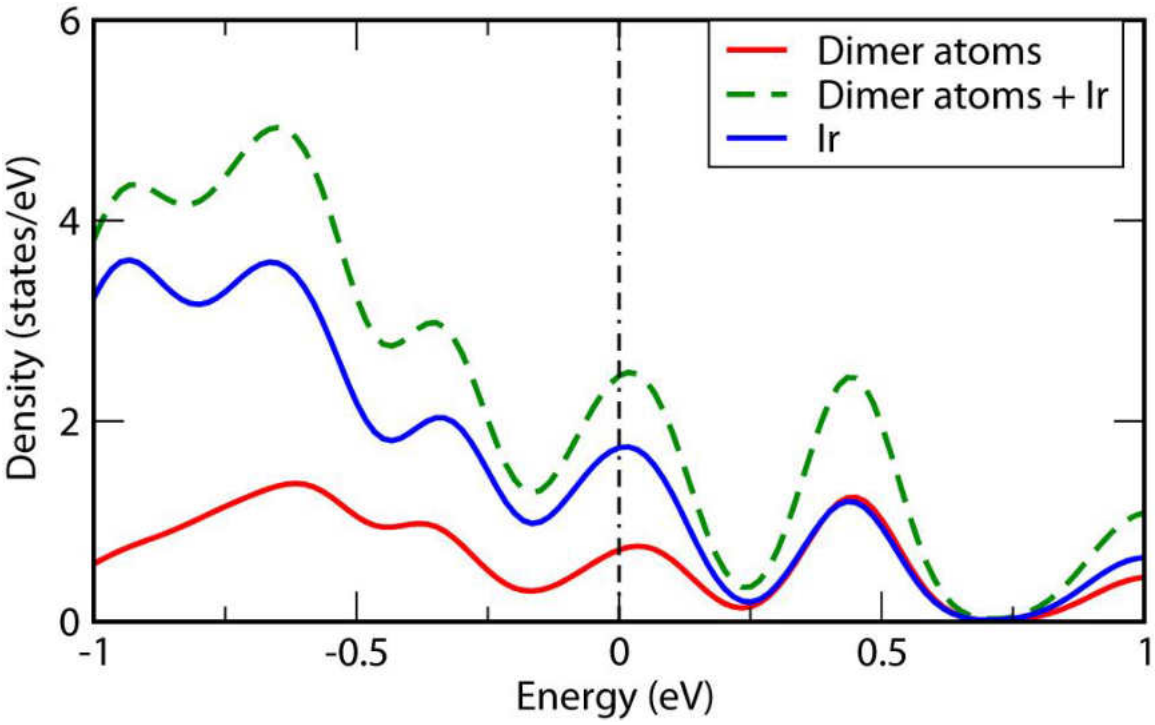

Figure 11. Calculated projected DOS curves of the proposed model.

the surface have ellipsoid peaks. Since the Ir atom is closest to the STM tip, it dominates the calculated STM images. Si dimers have significant DOS around Fermi level but they are located further away from the STM tip and their contribution to the tunneling current is small. However, the Si dimers are responsible for the elliptical shape of the peaks. For the

negative and the positive bias voltages, the major and minor axes of ellipses in the calculated STM images are swapped showing that upper and lower dimer atoms have different densities for occupied and unoccupied states around Fermi level. In measured STM images (see Figure 8b and 8c), the direction of the major axis of the ellipsoid is independent of the DOS sample bias and it is along the dimer row direction.

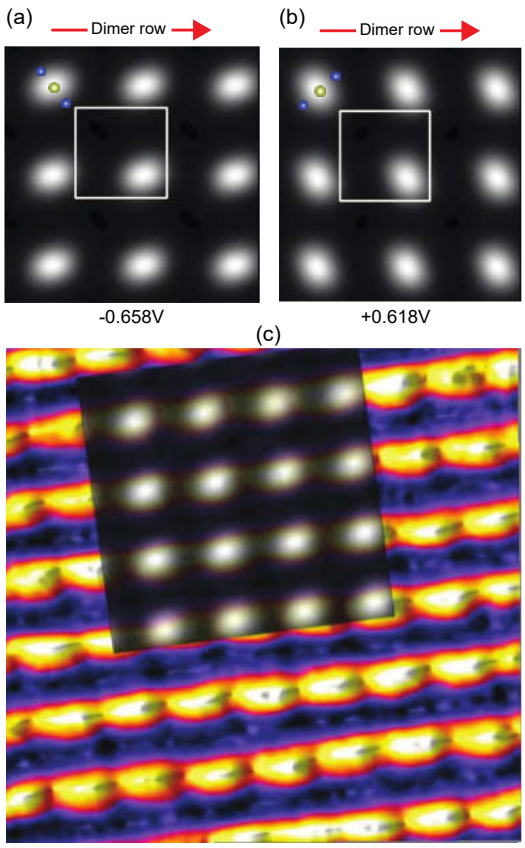

Figure 12. Simulated STM image for bias voltage of (a) -0.658 V and (b) 0.618 V. Blue atoms mark the dimer Si atoms that do not contribute STM images. White squares enclose a 2x2 surface cell. The red arrows show the direction of dimer row. (c) Background: A 15 nm × 15 nm STM image of Ir-silicide nanowires, sample bias and tunneling current are -0.658 V and 0.68 nA. The inset is the calculated STM image.

We attribute this to the fact that in the theoretical model the Si dimers are fixed however in reality, the dimers can flip. It is known that on pristine Si(001) surface, at temperatures above ~200 K, Si dimers constantly flip which causes dimers appearing as oblong protrusions in measured STM images leading to characteristic 2×1 structure[72]. A similar flipping motion would lead to an STM image that sees the averaged DOS on dimer atoms and tunneling through these flipping dimers make the peak elongate along the dimer row direction.

4.3: Conclusion

In conclusion, we studied the structural and electronic properties of Ir-silicide nanowires with STM/STS and DFT. The Ir atoms are found to sit at the top of the dimer row. DOS calculations and measured dI/dV curves show that the nanowires are metallic. Both measured and calculated DOS curves show that there are three well-resolved states around the Fermi level. The states at -0.55 eV and -0.13 eV carry large contributions from Ir atoms however state at 0.46 eV has equal contribution from Si dimers and Ir atom. While the Ir atoms mainly dominate the STM images, Si dimers also have noticeable contribution.

CHAPTER V

OCTANOIC ACID MODIFIED GRAPHITE SURFACE

Self-assembly of organic molecules is a widely studied since self-assembly offers a convenient approach for building organic molecule based electronic devices such as sensors, light-emitting diodes, photovoltaic cells. [78, 79] They can also function as corrosion inhibitor layers and chirally selective heterogeneous catalyzers. The quality of the molecular film and the interfaces between them are important as the performance of the devices depend on them. Molecule-substrate and molecule-molecule interactions are the two main factors that control the self-assembly. In order to reveal true nature of molecule-molecule interactions and avoid complications due to strong molecule-surface interactions, self-assembly of organic molecules are usually investigated on HOPG (Highly Ordered Pyrolytic Graphite) surface. STM (Scanning Tunneling Microscopy) is commonly used to study morphology of the molecular films and to characterize their electronic properties with sub-molecule resolution. [80,81] The interactions between molecules range from weak and non-directional van der Waals bonds to strong and directional hydrogen bonds. Hydrogen-bonding and van der Waals interactions are weaker than regular chemical bonds. The inherent weakness of these physical interactions may not always be strong enough to form stable structures. The selectivity and directionality of hydrogen

bonding can be used to tailor nanostructures by specific design of building blocks.[82, 83, 84] In that respect, the process resembles interlocking plastic toys.

Most of the time, self-assembly of organic molecules is studied at the solid-liquid interface which provides a gentle environment to deposit frail organic compounds.[85] Self-assembled monolayers of organic molecules dissolved in octanoic acid have been studied extensively. Octanoic acid can incorporate itself to the self-assembled structure by co-adsorbing together with the target molecule.[86] It has been suggested that the co-adsorption is motivated to increase hydrogen bond density of the self-assembled mono-layers on HOPG.[87] However, to the best of our knowledge, it has never been reported that octanoic acid molecules alone can form a thin film on a surface. In this study, we actually show that octanoic acid molecules by themselves can form a stable self-assembled molecular film on HOPG surface.

5.1: Experiment

HOPG substrates and Platinum-Iridium wire tips ($Pt_{0.8}$ $Ir_{0.2}$, 0.25 mm diameter) for STM were purchased from Nanoscience Instruments. Octanoic acid ($\geq 99\%$) was purchased from Sigma-Aldrich. Octanoic acid was used without further purification. Before each measurement, the samples were prepared by placing a droplet of octanoic acid on freshly cleaved basal plane of HOPG substrate and allowing appropriate time (~ 10 min.) for formation of monolayer. During the process, we made sure that the solvent was not dried out. All experiments were conducted under ambient conditions and at solid-liquid interface with the NanoSurf Easyscan-2 STM. The LDOS curves (normalized conductance

curves) were calculated from the measured I(V) curves and compared to theoretical calculations.

Theory:

All theoretical calculations were performed within plane-wave pseudopotential method based on Density Functional Theory as implemented in the PWscf code of the QUANTUM ESPRESSO package. [88] By using a projected augmented wave method within the PBE scheme, the Perdew–Burke–Enzerhof (PBE) exchange-correlation potential was approximated. [89] The single electron states were expanded in plane-waves and the kinetic energy cutoffs for the wave function was used $47\ Ry$. Only four layers of graphite sheet was considered in order to keep the unit cell manageable. To avoid the spurious interaction between periodic images, we used the vacuum space along z-direction is $\sim 14\ A°$. The length of unit cell along x and y directions are $26.97\ A°$ and $8.51\ A°$ respectively. For geometry optimization process, the maximum force allowed on each atom was $0.01\ au$ and between the consecutive self-consistent field calculations the convergence criteria for total energy was $10^{-6}\ au$. The density of states (DOS) calculations and the self-consistent calculations were performed on 5×5×1 grid. Test calculations showed that four layers of graphite were sufficient to describe (0001) surface. All the carbon atoms in graphite slab were fixed but the atoms forming octanoic acid molecules were allowed to relax.

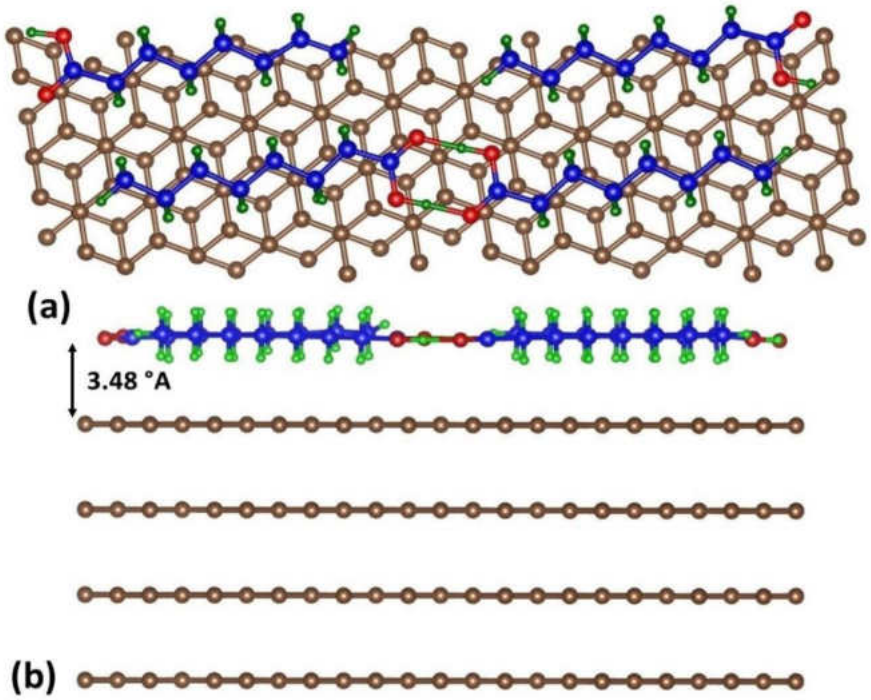

Figure 13. Proposed model of self-assembled monolayer of octanoic acid on HOPG. Carbon atoms of HOPG are in grey. Carbon, oxygen and hydrogen atoms of octanoic acid molecules are in blue, red and green, respectively.

5.2: Results and Discussions

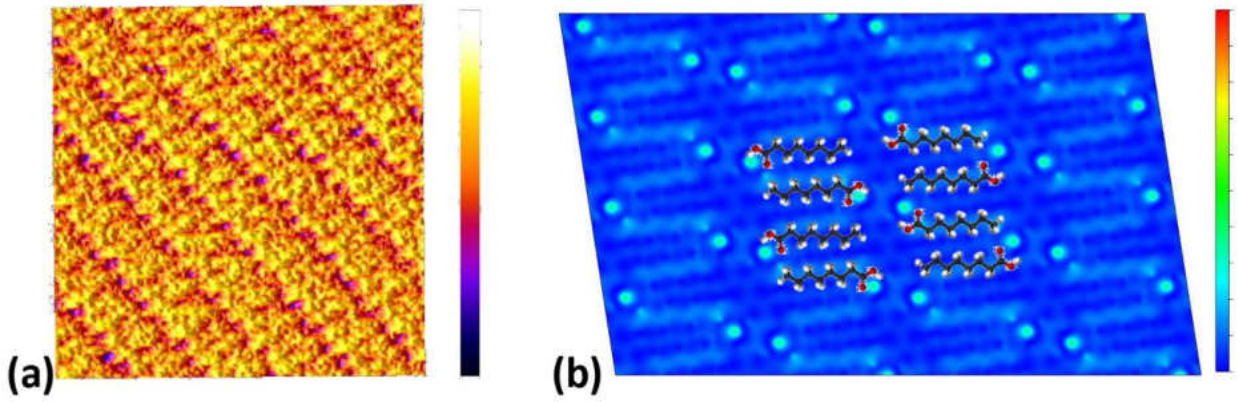

Figure 14. (a) An 8 nm × 8 nm STM image of octanoic acid on HOPG surface, V= -1.1 V, I= 0.7 nA. (b) Calculated STM image of octanoic acid on HOPG surface (V=-1.1 V). A model of the octanoic acid is overlaid on the STM image for clarity.

Figure 14 (a) is a high resolution STM image of octanoic acid adsorbed on HOPG surface. The HOPG surface was uniformly covered by the octanoic acid molecule. The average distance between repeating head groups is around 1.0 ± 0.1 nm. The angle between head group to chain angle is 87° ± 5°. To maximize the van der Waals interactions between the molecules, two adjacent octanoic acid molecules in a domain assemble with opposite faces. The -COOH group of each octanoic acid molecule form hydrogen bonds with its neighbor. Figure 14 (b) shows calculated STM image of the surface. The calculated STM image shows well-pronounced -COOH groups and well-resolved zigzags of $-CH_2$ groups. However, in the experimental STM image, the location of -COOH groups are not clearly visible and the resolution of the STM image is not good enough to pinpoint individual $-CH_2$ groups. It has been shown that STM images of similar molecules with longer $-CH_2$ groups measured under similar conditions had better resolution. [90,91] We attribute this lack of better resolution to the fact that octanoic acid molecules, because of their a short $-CH_2$ tail, are weakly attached to the surface and therefore they are somewhat mobile while scanning.

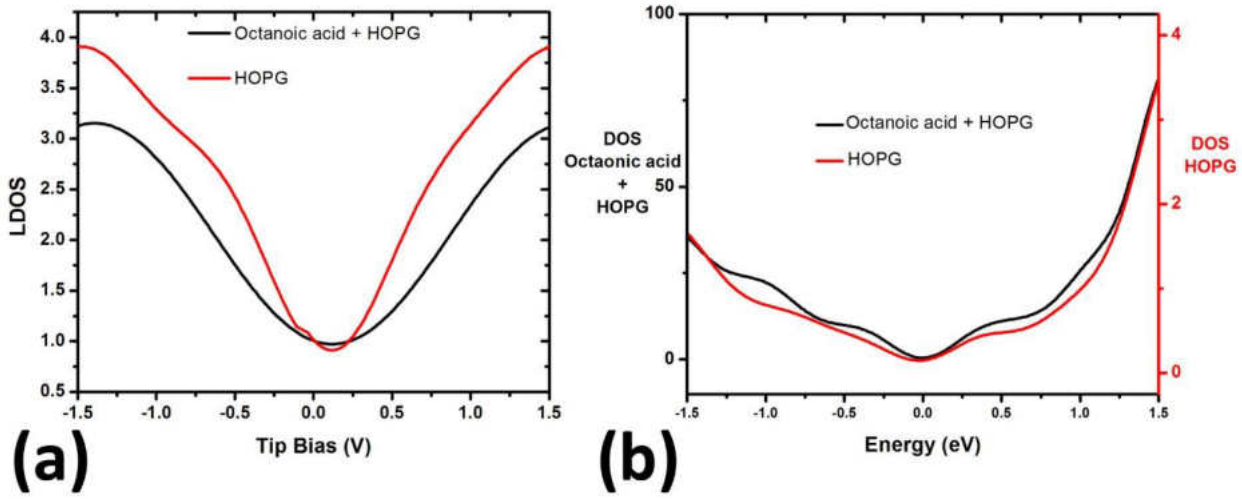

Figure 15. (a) LDOS graphs of Octanoic acid + HOPG (black curve) and HOPG (red curve) calculated from experimental I(V) curves. (b) Theoretical DOS graphs of Octanoic acid + HOPG (black curve) and HOPG (red curve). Note that the left (black) and the right side (red) of figure (b) has different scales.

Fig. 15(a) shows LDOS curves measured on pristine HOPG and octanoic acid covered HOPG surfaces, respectively. The comparison of these two graphs reveals that both of the surfaces are metallic. The LDOS graphs are almost identical around Fermi level which can be attributed to the fact that octanoic acid molecules are only physisorbed and they don't modify the surface chemistry of HOPG. It also indicates that octanoic acid molecules have no states around Fermi level to contribute to the tunneling current. In Fig. 15b, we compare the theoretical density of states curves calculated for both pristine HOPG and octanoic acid adsorbed HOPG surface. Both DOS curves look pretty similar around Fermi level which confirms experimental data. In order to see the contribution of octanoic acid to the DOS, we calculated projected DOS of octanoic acid molecules (see 16a). As expected, the DOS of octanoic acid has a band gap around Fermi level (roughly between − 2 eV to 2.4 eV) supporting the discussion presented above.

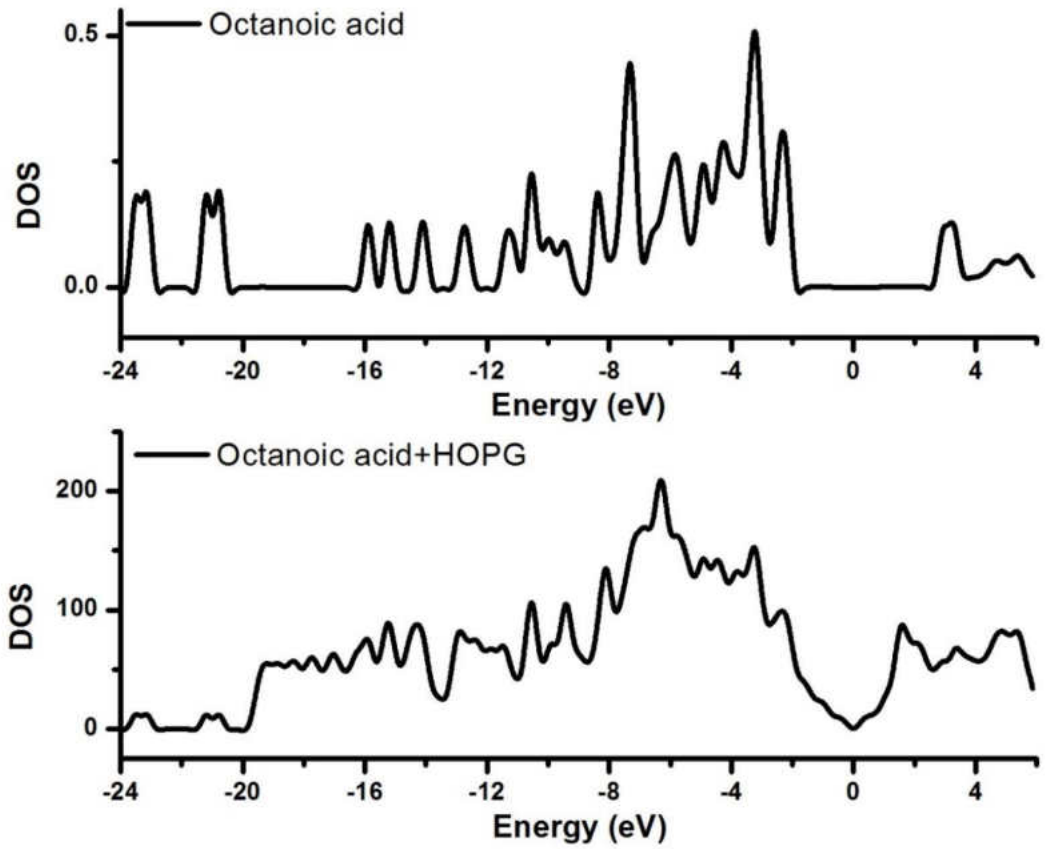

Figure 16. (a) Projected DOS of octanoic acid molecules. The molecule has a band gap between − 2 eV to 2.4 eV. (b) DOS of octanoic acid and HOPG together.

5.3: Conclusion

In summary, we studied structural and electronic properties of self-assembled monolayer of octanoic acid molecules formed on HOPG surface with STM/STS and DFT. The LDOS curves measured on octanoic acid and on pristine HOPG surface show similar features. We attribute this to the fact that octanoic acid molecules physisorbed on HOPG surface. Albeit the measured STM images have limited resolution, they show great resemblance to the calculated STM images confirming the validity of the proposed model. The take away message of the paper is that the role of solvent molecules in self-assembly may go beyond co-adsorption.

CHAPTER VI

IRIDIUM ON SILICON (111) SURFACE

Transition metal-silicon interfaces are technologically important because metal silicides form rectifying junctions with various Schottky barrier heights. Among those, Iridium/silicon interface is unique because of its lowest (highest) Schottky barrier for holes (electrons). That's why they are perfect for metal oxide semiconductor devices (MOSFET's)[92,93]. Beside their technological importance, metal-silicon interface offers a unique chance to explore growth of heteroepitaxial thin films. The transition metals and silicon form complex structures by strong interaction. The bulk properties of iridium-silicides epitaxially grown on Si(100) and/or Si(111) has been studied extensively [94,95,96,97,98]. The enthalpy of mixing between Ir and Si atoms is negative leading to solid-state amorphization[99,100]. Ir-silicide bulk have three known crystal phases and each silicide grows in a specific temperature range and only one silicide phase grows at a given temperature. No crystallization forms if the sample is annealed below $410°C$. A semi-amorphous Ir_3Si_5 phase forms when annealing temperature is in between $410°C$ and $660°C$. For annealing temperature between $660°C$ and $720°C, IrSi$ phase forms. IrSi completely disappears when annealing temperature is above $720°C$. When annealing temperature is $1080°C$, $IrSi_3$ phase forms[101,102]. Recently, both our work on Ir/Si(001) system and Hormann et. al.'s work showed that Ir-modified Si surfaces has a tendency to grow fluorite-type $IrSi_2$ which has not been observed in bulk.[103,104] Ir modified Si(111)

surface for small Ir coverage were studied with scanning tunneling microscopy/spectroscopy (STM/STS), angle resolved photoemission spectroscopy and density functional theory calculations by our group. [105,106] In this chapter, we present our experimental results on what happens to Ir modified Si(111) surface at higher Ir concentration.

6.1: Experiment

The Si (111) samples were cut from nominally flat $76.2mm \times 0.38mm$, single side-polished n-type (phosphorous doped) wafers. The samples were mounted on molybdenum holders carefully avoiding contact of the samples to any other metal during preparation and experiment. The STM/STS measurements were performed by using an ultra-high vacuum (UHV with a base pressure of $2 \times 10^{-10}\ mbar$) equipped with an Omicron variable temperature STM and a LK technologies RVL2000 LEED-Auger system. All the experiments were performed at room temperature and the base pressure was always kept below $5 \times 10^{-10}\ mbar$ during the experiments. Samples were washed with isopropanol and dried under the flow of nitrogen gas before introducing them in to the UHV chamber. The Si (111) samples were degassed extensively followed by flash annealed at $1250°C$. The quality of the clean Si (111) samples was confirmed with STM before depositing Ir. Over the clean Si (111)-7 × 7 sample, Ir was deposited from a current heated wire (99.9%). While taking high-resolution STM images of the surface, $I - V$ curves were measured.

6.2: Results and Discussions

Figure 17 (a) shows an STM image of clean Si(111)-7 × 7 surface. After cleaning the sample we deposited Ir and anneal the sample at 750℃. Most of the surface is covered by $\sqrt{7} \times \sqrt{7} - R19.1°$ domains (hereafter as $\sqrt{7} \times \sqrt{7}$). The domains that make the $\sqrt{7} \times \sqrt{7}$ domains are called Ir-ring clusters. Any Ir coverage bigger than 1/7 th of a monolayer would

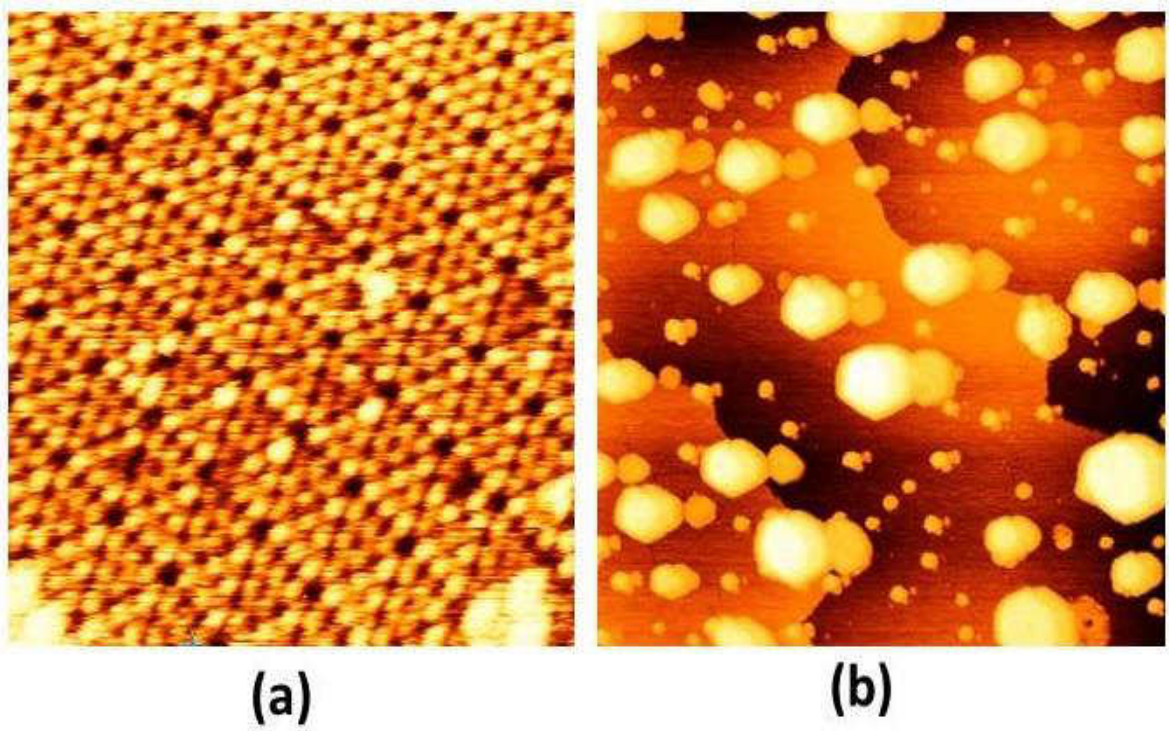

Figure 17. (a) $20\ \text{nm} \times 20\ \text{nm}$ STM image of Si(111)- 7×7, $\text{V} = -1.312\ \text{V}$, $\text{I} = 0.688\ \text{nA}$. (b) $250\ \text{nm} \times 250\ \text{nm}$ STM image of Ir-modified Si (111) surface, $\text{V} = -0.822\ \text{V}$, $\text{I} = 0.25\ \text{nA}$.

Figure 18 (a) shows a higher resolution STM image of the $\sqrt{7} \times \sqrt{7}$ domains. According to the ring cluster model (see Figure 18b), Si atoms of the top substrate layer are substituted by the Ir atoms which makes each Ir atom surrounded by six Si atoms, three of which are called bridging adatoms and they directly bind to the Ir atom and the remaining three Si atoms are called the capping adatoms which bind to two bridging adatoms and one Si substrate atom. The most crucial difference between a capping and bridging Si adatoms is that all the bonds of the bridging Si adatoms are saturated whereas the capping adatoms have a dangling bond. Additionally, the capping adatoms are located slightly higher than the bridging adatoms. In the filled state image, the ring-cluster appears as a single protrusion because the filled-states must have significant contribution from the Ir atom at the center of the ring cluster[41].

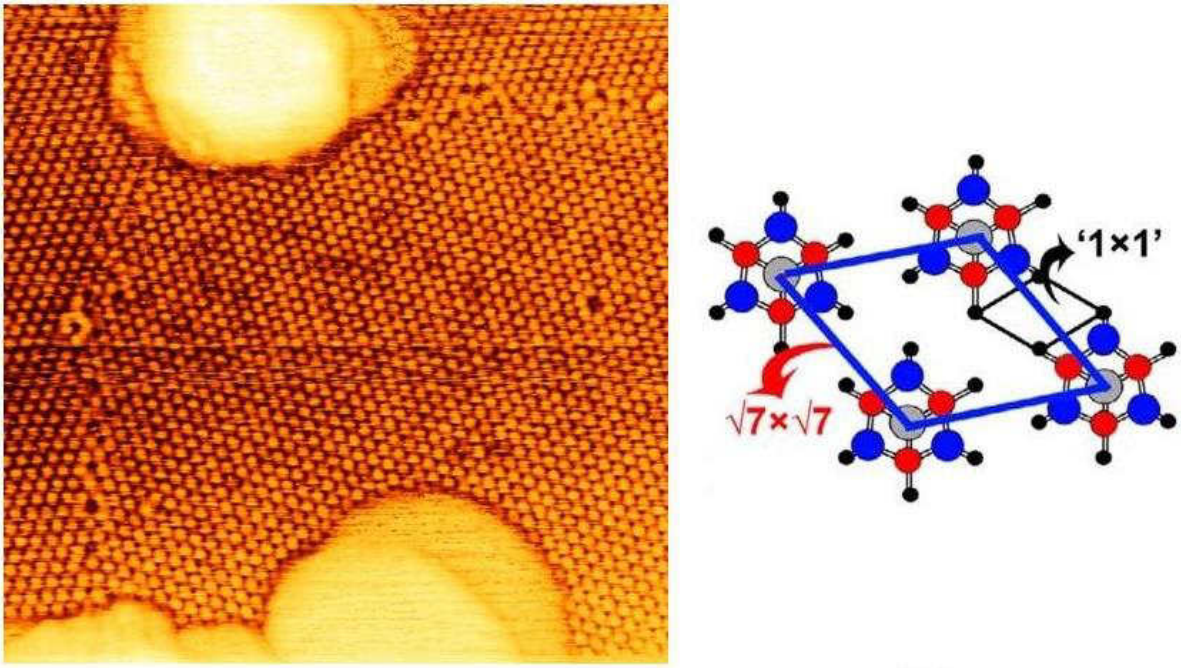

Figure 18. (a) Ir-ring cluster on $100\ \text{nm} \times 100\ \text{nm}$ STM image of Si(111)- 7×7, $V = -1.235\ V, I = 0.414\ nA$. (b)Schematic of Ir-ring cluster with blue and red dots representing the capping and bridging adatoms, respectively.

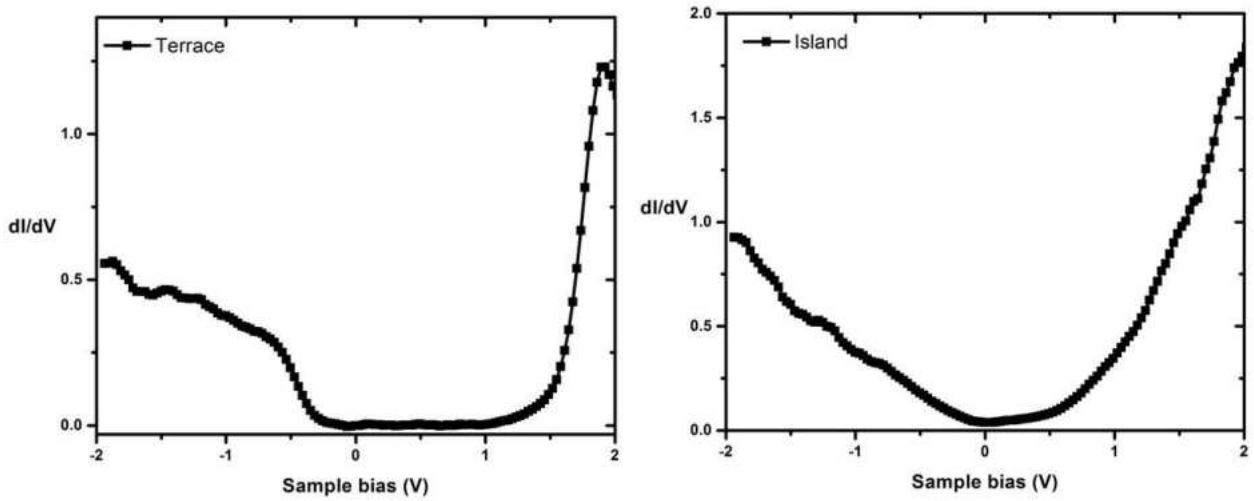

Figure 19. dI/dV curves measured on (a) $\sqrt{7} \times \sqrt{7}$ domain, and (b) Ir islands.

The dI/dV curves were obtained by numerically taking derivative of the I-V curves. The dI/dV curves measured on $\sqrt{7} \times \sqrt{7}$ domains has a band gap around the Fermi level. On the other hand, the dI/dV curve measured on the islands has nonzero conductance around the Fermi level indicating that the islands are metallic. STM images measured on the islands do not reveal any atomic structure indicating that the islands can be amorphous Ir.

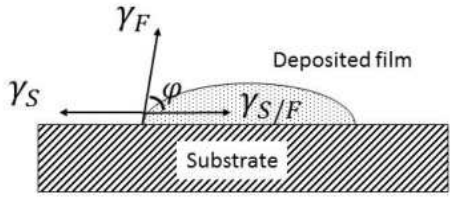

Figure 20. A simple model showing surface free energies. γ_S, γ_F and $\gamma_{S/F}$ are the surface free energies between the substrate and vacuum interface, deposited film and vacuum interface, substrate and film interface, respectively.

Under current growth conditions, the islands prefer to grow vertically (Stranski–Krastanov type, layer+island growth) and Ir-ring clusters ($\sqrt{7} \times \sqrt{7}$ domains) function as a wetting layer. We can explain growth modes in terms of surface free energy. Surface free energy is the energy necessary to create an additional piece of a surface or an interface. Surface free energy can be also considered as force per unit length of boundary. Force equilibrium at a point where substrate and three-dimensional island formed by the deposited film make contact requires the following equation: [107]

$$\gamma_F \cos(\varphi) + \gamma_{S/F} = \gamma_S$$

Where, γ_S, γ_F and $\gamma_{S/F}$ are the surface free energies of the substrate-vacuum interface, deposited film-vacuum interface and substrate-film interface, respectively. (see Figure 6.4) For layer-by-layer growth, $\varphi = 0$ and $\gamma_F + \gamma_{S/F} \leq \gamma_S$. On the other hand, for island growth, $\varphi > 0$ and $\gamma_F + \gamma_{S/F} > \gamma_S$. For Ir/Si(111)system, we have Stranski-Krastanov growth mode which is a result of lattice mismatch between deposited film and substrate. The lattices of the film and the substrate deform in such a way that they minimize lattice mismatch. However, this deformation causes extra stress and changes the growth mode from layer-by-layer to island mode. Since $\sqrt{7} \times \sqrt{7}$ domains and bulk Ir is incommensurate, there must be significant strain at the interface between the islands and $\sqrt{7} \times \sqrt{7}$ domains. It is hard to predict the actual interface however; it is highly plausible that Ir atoms and the capping adatoms (with dangling bonds) of ring clusters form the bonding between islands and the $\sqrt{7} \times \sqrt{7}$ domains. Most of the islands are hexagonal suggesting that they are (111) plane, but sometimes a couple of them come together to form islands

with irregular shapes (see Figure 17b). Figure 21 shows average diameter (a) and average height (b) of Ir islands as a function of coverage calculated for up to 1 ML Ir.

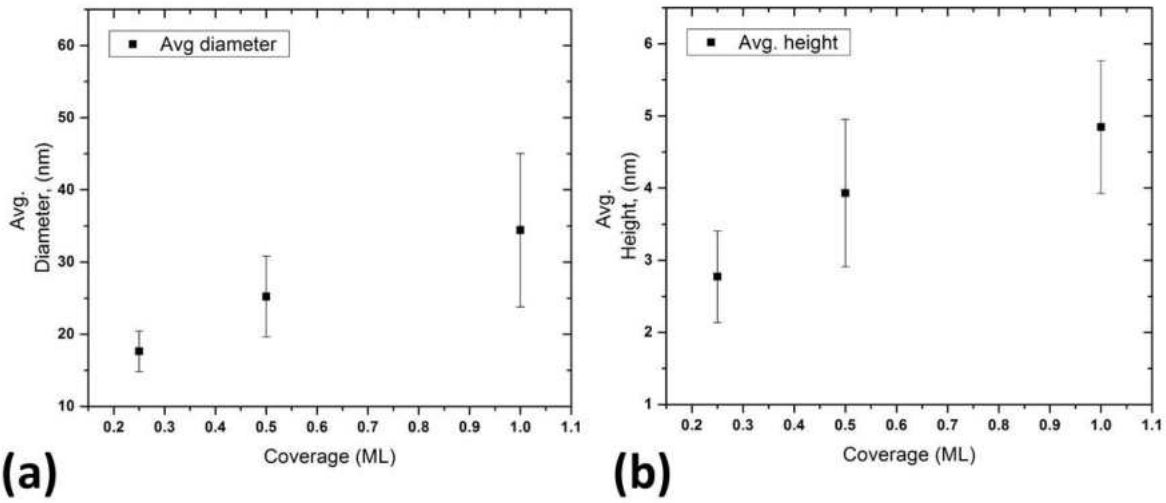

Figure 21. Average diameter and Average height of the islands as a function of Ir surface coverage.

6.3: Conclusions

Ir deposited on Si (111) surface was extensively studied with STM/STS measurements. The dI/dV curves measured on the islands show no band gap around the Fermi level, on the other hand, dI/dV curves measured on $\sqrt{7} \times \sqrt{7}$ domains exhibit a bandgap around the Fermi level. Depositing of Ir up to 1ML coverage, increases both the diameter and the height of the islands indicating that thin film follows Stranski–Krastanov type growth mode.

CHAPTER VII

1-DECANETHIOL MODIFIED SILICON (110) SURFACE

Self-assembled monolayers (SAMs) have attracted considerable attention because of their potential applications in a variety of fields such as biosensors, lithography, and electrochemistry[108] . To control modifications of surface properties such as wettability, adhesion, lubrication, and corrosion, SAMs with properly chosen functional groups are important[109]. SAMs have very important aspect that by bonding particular chemical groups at the free end of the alkyl-thiol moieties, it can confer chemical, electronic, optical or biological to the substrate. This can be done by selecting substituents that are able to form covalent and non-covalent bonds[110]. To understand thiol-based SAMs structures Scanning Tunneling Microscopy (STM) has been commonly used. Usually, STM measurements perform either at the solid-liquid interfaces or under UHV conditions.

In the present study, we have investigated the physical and electronic properties of 1-decanethiol SAM on Ir modified Si (110) surface at the solid-liquid interface using NanoSurf Easyscan-2 STM. We also studied chemical properties of the sample with the help of X-ray photoelectron spectroscopy (XPS).

7.1: Experiment

Iridium-modified silicon (110) surface was used as a substrate. Iridium (99.9%) wire and Si(110) wafer were purchased from Goodfellow. Silicon (110) surfaces was cut from

nominally flat, both sided polished n-type (phosphorous doped, R=0.05-0.5 Ohm-cm) wafers. The sample was mounted on molybdenum holders, during preparation and experiment contact of the samples to any other metal were carefully avoided. The UHV-STM is equipped with low energy electron diffraction (LEED) and STM. The base pressure of UHV system was less than $2 \times 10^{-10}\, mbar$. The XPS experiments were conducted in a PHI-5400 XPS system with Ar^{+} sputter gun and a base pressure of $2 \times 10^{-10} mbar$. Before depositing Ir, Si(110) were degassed extensively followed by a flash annealing cycle at $1250°C$. Ir was deposited over the clean surface from a current heated Ir wire. After deposition at room temperature, the samples were annealed at $800°C$ to form flat Ir terraces.

1-Decanethiol ($CH_3(CH_2)_8CH_2SH$) and ethanol were purchased from Sigma-Aldrich and used without further purification. 1-Decanethiol monolayers on Ir-modified Si (110) substrates were prepared at room temperature under ambient conditions by immerging the substrates into 1mM ethanol solutions for 24 hours. Then the sample was inspected by STM. All STM experiments were conducted under ambient conditions with the NanoSurf Easyscan-2 STM. While measuring STM images, $I(V)$ curves on the surface were measured. Platinum-Iridium wire tips (Pt0.8 Ir0.2, 0.25 mm diameter) for STM were purchased from Nanoscience Instruments. In order to study the elemental composition of the surfaces, the sample transferred to the XPS chamber. The sample was measured by an $Al\ K\alpha\ (1486.6\, eV)$ X-ray source for survey and high-resolution scan with pass energies of $89.5\, eV$ and $8.95\, eV$ respectively. All the XPS core level spectra were analyzed with least-squares minimization curve fitting program. Si (Ir) core-level peak was fitted

using a symmetric (asymmetric) Gaussian instrument response function convolved with Lorentzian core-level line shape (GL). For both Ir 4f and Si 2p peaks, the secondary electron background was subtracted using a Shirley function. [111]

7.2: Results and discussions

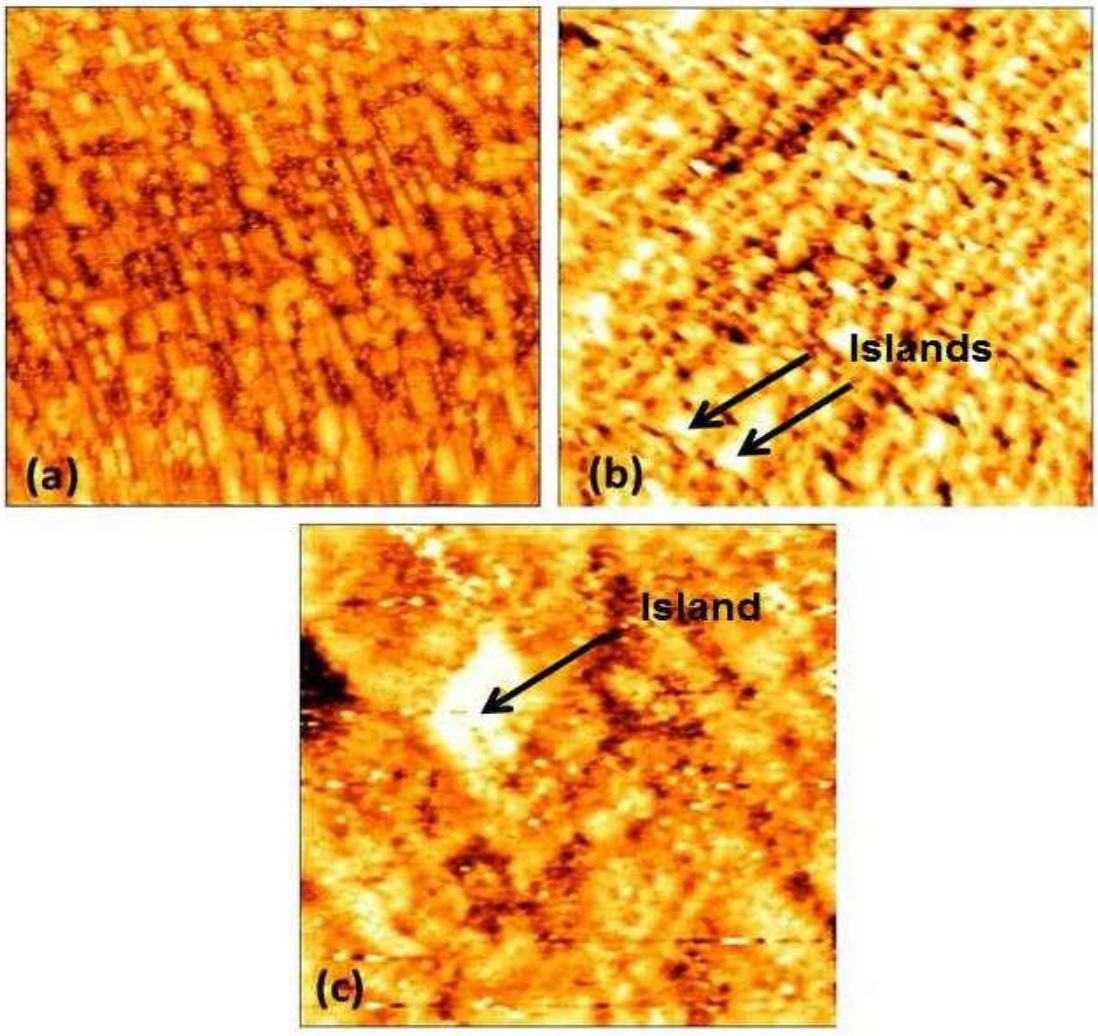

Figure 22: (a) An 100 nm × 100 nm STM image of Iridium modified Si (110) surface taken at UHV conditions, $V = -1.18\,V, I = 0.234\,nA$. (b) An $400\,nm \times 400\,nm$ STM image of 1-decanethiol on Iridium modified Si (110) surface, $V = 1\,V, I = 0.1\,nA$. (c) An $100\,nm \times 100\,nm$ STM image of 1-decanethiol on Iridium modified Si(110) surface, $V = 1\,V, I = 0.1\,nA$. Both of the images (a) and (b) were taken at ambient conditions

Figure 22(b) and (c) shows the STM images of 1-decanethiol SAMs on Ir-modified Si (110) surface. Images taken at larger scale are shown in Figure 22(a). It reveals that 1-decanethiol monolayer formed on the surface with small islands and vacancy of islands[112]. There is a contrast variation in the area between the substrate islands.

dI/dV curves were calculated from the measured $I(V)$ curves. We didn't see any band gap around the Fermi level on the islands and in between the islands meaning that the whole surface is metallic. One curious difference between the dI/dV curves was the enhanced conductance measured in between the islands. We attributed this to the absence of 1-decanethiol molecules on the surface. Between the islands, exposed Si surface was expected to form a thin oxide layer. Depending on the thickness the band gap of silicon oxide changes from 1.1 eV to 9 eV. [113] Absence of any band gap indicates that the areas in between the islands are in some form of Ir-silicide which can be metallic. In order to get more information about the surface chemistry, XPS measurements were performed.

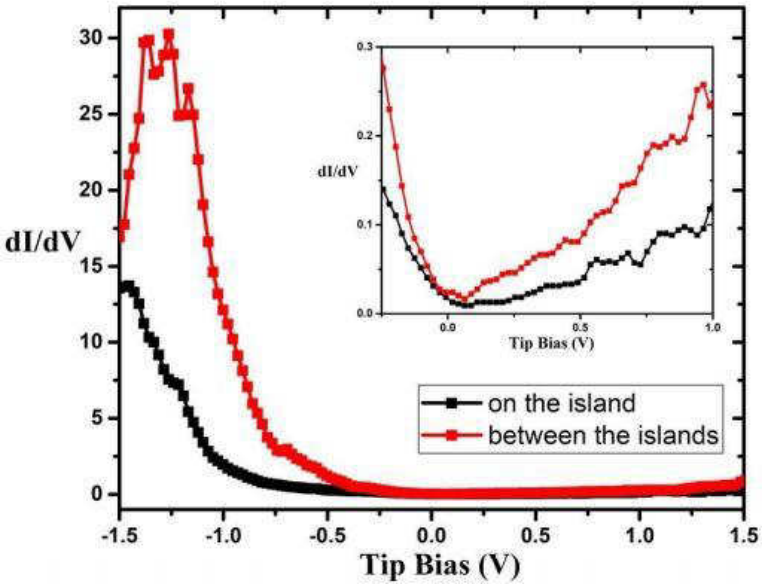

Figure 23. dI/dV curves of 1-decanethiol + Iridium modified Si(110) surface calculated from $I(V)$ curves taken on the island (black) and in between the islands (red). Inset shows a zoomed in part of the main dI/dV to show dI/dV curve better around the Fermi level.

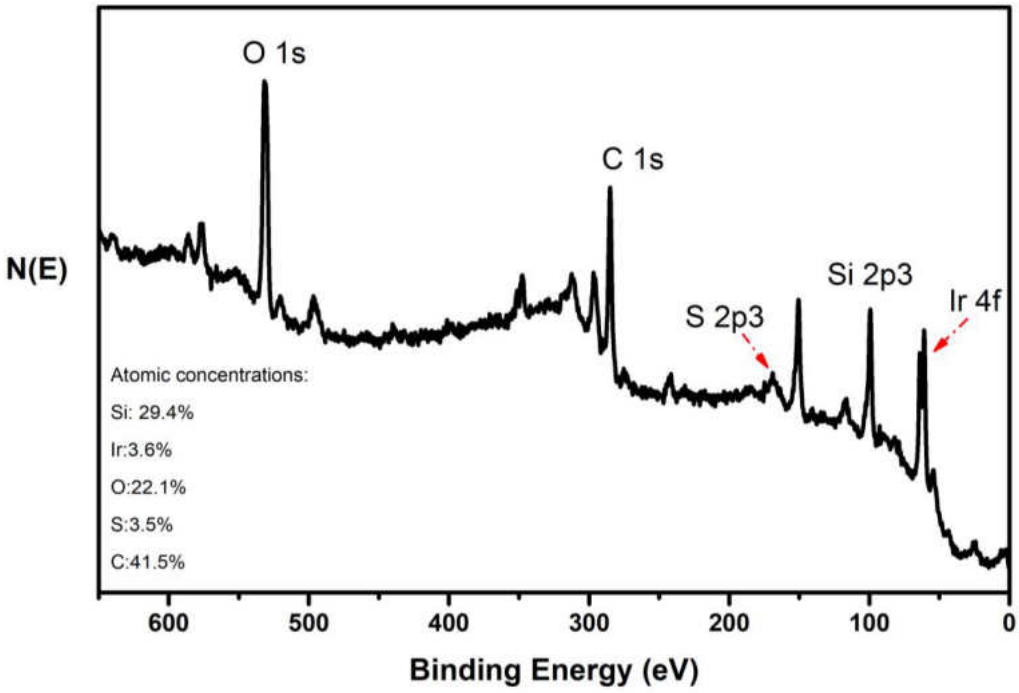

Figure 24. An XPS spectrum of 1-decanethiol on Ir modified Si (110) surface where we can see the coverage of the surface.

Multiple elements were identified in XPS survey measured on 1-decanethiol modified Ir/Si (110) surface. (Figure 24) According to the incident X-ray energy, the abscissa was adjusted so as to reflect the binding energy of the detected core-shell electrons. Different elements and their associated core energy levels are indicated in the spectrum[114]. All the expected elements appear in the XPS survey spectrum (Si, Ir, O, C and S)[115]. Sulfur to carbon ratio is 0.083 which is very close to sulfur to carbon ratio in 1-decanethiol molecule which is 0.1.

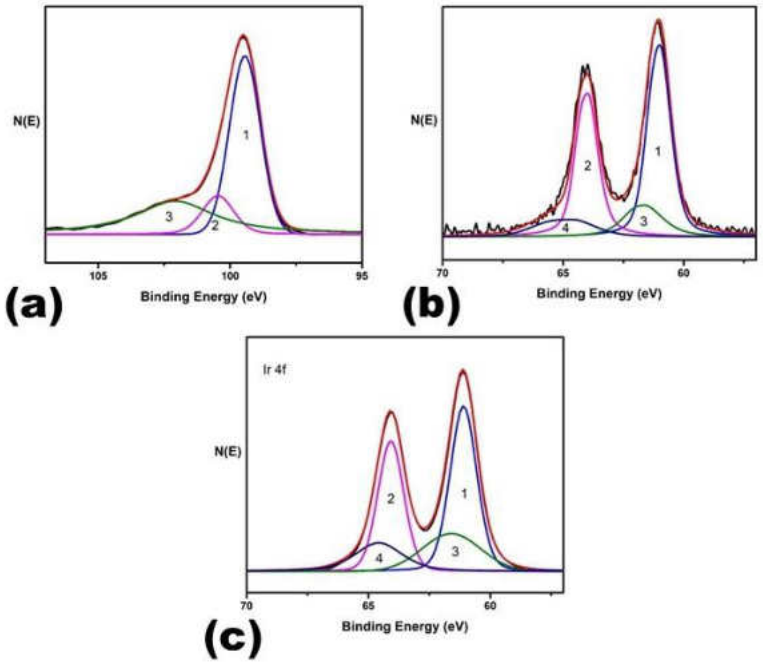

Figure 25 shows (a) Si 2p peak measured on 1-decanethiol+ Ir-modified Si surface. (b) Ir $Ir4f$ peaks measured on Ir-modified Si(110) sample (b) $Ir4f$ peaks measured on 1-decanethiol+ Ir-modified Si surface.

Si 2p measured on 1-decanethiol modified Ir-modified Si (110) sample has three components, bulk Si at 99.45 eV (peak 1), Si in Ir-silicide at 100.46 eV (peak 2) and silicon oxide 102.08 eV (peak 3). The binding energy of both peak 1 and 2 are in line with previ-

ous measurement on pristine Ir modified Si(110) surface.[116] Peak 3 is new for this substrate and proved the existence of oxide formation on the surface. Figure 25 (b) and (c) shows Ir 4f peaks measured on QDs/Si (110) sample and on 1-decanethiol modified Ir-modified Si (110) sample. Ir 4f peaks exhibit spin-orbit splitting fitted with four Gaussian-Lorentzian peaks to represent the two doublets originating from Ir-bulk and Ir-silicide. Both the energy difference and the area of the $4f_{5/2}$ peaks (peaks 2&4) were fixed with respect to the $4f_{7/2}$ peaks (peaks 1&3). The binding energy of the $4f_{5/2}$ peaks were set 2.98 eV higher than that of the $4f_{7/2}$ peaks and the area ratio between them were kept 3:4. The binding energy of $4f_{7/2}$ peaks (1^{st} peaks) are about 61 eV and they are in-line with the literature.[9] The full-width at half maximum (FWHM) of 1st peaks are at 1.23 eV & 1.29 eV for QDs/Si (110) sample and 1-decanethiol modified Ir-modified Si (110) sample, respectively. Since both the position and the FWHM values of these peaks are close, it suggests that these peaks are originating from bulk Ir. In addition to that, the positions of the 3^{rd} peaks (about 61.60 eV) are very close. However, the FWHM of the 3^{rd} peaks are quite different. (2.14 eV vs. 2.81 eV for QDs/Si (110) sample and 1-decanethiol modified Ir-modified Si (110) sample, respectively) The higher value of FWHM of latter is attributed to the attachment of thiol group to Ir atoms on the surface.

The C 1s and S 2p spectra on the 1-decanethiol modified Ir-modified Si (110) surface are shown in figure 26. Both peaks shift significantly to higher binding energies. The C 1s peak measured on $CH_3(CH_2)_{15} - SH/Au$ self-assembled monolayer is located at 284.97 eV.[117] On our sample, C 1s peak is located at 285.15 eV. This type of shift in C 1s peak is observed on alkanethiols with groups like –COOH or -CH_2OH indicating the for-

mation of oxide. Similarly, S 2p peak measured on $CH_3(CH_2)_{11} - SH/Au$ is located at 162.3 eV. [118] However, S 2p of our sample is located at 168.43 eV which is significantly in higher binding energy. S 2p shifts to such high binding energies were observed only if there is sulfur oxygen bonding which supports the idea that there is some oxidation on the surface. [119]

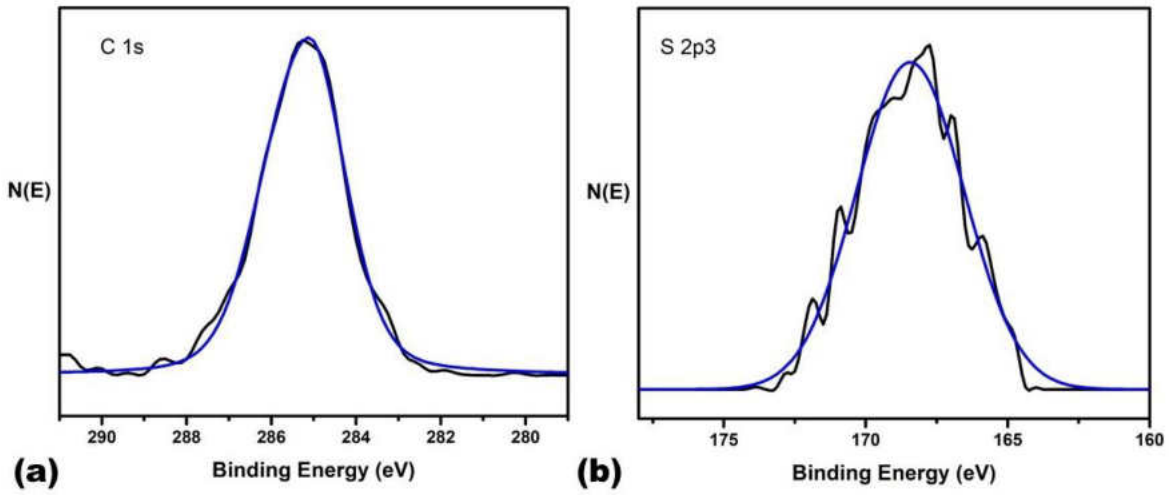

Figure 26. shows (a) $C1s$ peak, and (b) $S2p$ peaks measured on 1-decanethiol+ Ir-modified Si (110)surface.

7.4: Conclusions

1-decanethiol on Ir modified silicon sample was extensively studied with STM/STS and XPS measurements. Measured dI/dV graphs shows no band gap around the Fermi level indicating the metallic nature of the surface. XPS data confirms the formation of 1-decanethiol SAMs on Ir modified Si (110) surface.

CHAPTER VII

CONCLUSION

This dissertation focuses on two topics, metal induced changes in different cuts of silicon surfaces and molecular films on graphite and Ir modified Si (110) surface. However, all of these projects reveal an underlying theme self-assembly. The self-assembly is the functional components in integrated circuits. It increases the efficiency of electronic and photonic devices and reduces costs of consumer electronics. It is possible to create different self-assemblies out of atoms and molecules.

Experiments performed on molecular lamellae on highly ordered pyrolytic graphite in chapter VI and Ir-modified Si (110) surface on chapter VII is a motivation to study the effects of molecular adsorption on the technologically relevant surfaces of graphite and Si(110). The main inspiration behind these projects was to investigate whether it is possible to modify the electronic properties of graphite and Ir modified Si (110) surface by the physical adsorption of organic molecules. Carefully designed organic molecules can be used in various applications such as harvesting electronic sensors or solar energy. For these projects, we used octanoic acid and 1-decanethiol. It has been proved from STM measurements that these molecules were successfully adsorbed on assigned surfaces.

Ir-modified Si(111) and Si (001) surfaces were also investigated in this research. In ring clusters, there are six silicon atoms surrounding an Ir atom at the center. After coming together the ring clusters form $\sqrt{7} \times \sqrt{7}$ domains on the surface. This surface has band gap but scanning tunneling spectroscopy study reveals that the Ir-silicide islands are metallic.

On the other hand, by measuring STM images on Ir-modified Si(001) surface, it has been shown that the surface hosts Ir-silicide nanowires. STM images on the wetting layer near the Ir-silicide wires as well as on the neighboring Ir-silicide domains show that the nanowires form along the dimer rows of Si(100)-2×1. A proposed model for the Ir-silicide nanowires suggests that Ir atoms are found to sit at the top of the dimer row. Our study on Ir-modified Si (001) surface is almost complete but this research will inaugurate a strong foundation of future investigations on this surface.

REFERENCES

[1] Manuel Smeu, Hong Guo, Wei Ji, and Robert A. Wolkow, Phys. Rev. B 85, 195315 (2012).
[2] Feynmann, R. P. Eng. Sci., 23, 22, (1960).
[3] Pham, T. A. (2016). Constructing low-dimensional molecular networks on metal surfaces [Groningen]:University of Groningen
[4] V. Balzani, *Pure Appl. Chem*., 8, 1631, (2008).
[5] J. V. Barth, G. Costantini, K. Kern, Nature, 437, 671, (2005).
[6] J. V. Barth, Annu. Rev. Phys. Chem., 58, 375, (2007).
[7] M. Witmer, P. Oelhafen, and K. N. Tu, Phys. Rev. B 35, 17 (1987)
[8] Dubois, Emmanuel, and Guilhem Larrieu. "Low Schottky Barrier Source/drain for Advanced MOS Architecture: Device Design and Material Considerations." *Solid-State Electronics* 46.7 (2002): 997–1004.
[9] Larrieu, G. et al. "Formation of Platinum-Based Silicide Contacts: Kinetics, Stoichiometry, and Current Drive Capabilities." *Journal of Applied Physics* 94.12 (2003): 7801.
[10] S. Peterson, J. Baglin, W. Hammer, F. d'Heurle, T.S. Kuan, I. Ohdomari, J. de Soussa Pires, and P. Tove, J. Appl. Phys. 50, 3357 (1979).
[11] W. Knapen, J. Demeulemeester, D. Deduysche, J. L. Jordan-Sweet, A. Vantomme, R. L. Van Meirhaeghe, C. Detavernier, C. Lavoie, Microelectronic Engineering 87, 258 (2010).
[12] S. Peterson, J.A. Reimer, M. H. Brodsky, D.R. Campell, F. d'Heurle, B. Karlsson, and P. A. Tove, J. Appl. Phys. 53, 3342 (1982).
[13] M. Wittmer, P. Oelhafen, K.N. Tu, Phys. Rev. B. 33, 5391 (1986).
[14] Y. P. Zhang, L. Yang, Y. H. Lai, G. Q. Xu, and X. S. Wang, "Self-assembly of one-dimensional molecular nanostructures on the Ge-covered Si(100) surface"*Appl. Phys. Lett*. 84 (2004): 401.
[15] H. Okino, I. Matsuda, R. Hobara, Y. Hosomura, S. Hasegawa, and P. A. Bennett, "In situ resistance measurements of epitaxial cobalt silicide nanowires on Si(110)" *Appl. Phys. Lett.* 86 (2005): 233108.
[16] A. Kida, H. Kajiyama, S. Heike, T. Hashizume, and K. Koike, "Self-organized growth of Fe nanowire array on H_2O/Si(100)(2×n)" *Appl. Phys. Lett.* 75 (1999): 540.
[17] R. Losio, K. N. Altmann and F. J. Himpsel, "Continuous Transition from Two- to One-Dimensional States in Si(111)-(5×2)–Au" *Phys. Rev. Lett.* 85 (2000): 808.
[18] J. R. Ahn, H. W. Yeom, H. S. Yoon, and I. -W. Lyo, "Metal-Insulator Transition in Au Atomic Chains on Si with Two Proximal Bands" *Phys. Rev. Lett.* 91 (2003) 196403.
[19] Dabrowski, J. & Müssig, H.-J. Silicon Surfaces and Formation of Interfaces (World Scientific, Singapore, 2000).
[20] Chadi, D. J. Atomic and Electronic Structures of Reconstructed Si(100) Surfaces. *Phys. Rev. Lett.* 43, 43 (1979).
[21] Krüger, P. & Pollmann, J. Dimer Reconstruction of Diamond, Si, and Ge(001) Surfaces. *Phys. Rev. Lett.* 74, 1155 (1995).

[22] Yates, J. T., Jr. A new opportunity in silicon-based microelectronics. *Science* 279, 335–336 (1998).
[23] Medeiros-Ribeiro, G., Bratkovski, A. M., Kamins, T. I., Ohlberg, D. A. A. & Williams, R. S. Shape Transition of Germanium Nanocrystals on a Silicon (001) Surface from Pyramids to Domes. *Science* 279, 353–355 (1998).
[24] Wolkow, R. A. Controlled molecular adsorption on silicon: laying a foundation for molecular devices. *Annu. Rev. Phys. Chem.* 50, 413–441 (1999).
[25] Engelund, M. *et al.* Tunneling spectroscopy of close-spaced dangling-bond pairs in Si(001):H. *Sci. Rep.* 5, 14496 (2015).
[26] Qiu, Y. *et al.* Epitaxial diamond-hexagonal silicon nano-ribbon growth on (001) silicon. *Sci. Rep.* 5, 12692 (2015).
[27] B. S. Swartzentruber, N. Kitamura, M. G. Lagally, and M. B. Webb, Phys. Rev. B 47, 20 (1993).
[28] K. Yoo and H. H. Weitering, Phys. Rev. B 65 11542 (2002).
[29] Joost van der Lit, Jolien L. Marsman, Rik S. Koster, Peter H. Jacobse, Stephan A. den Hartog, Daniel Vanmaekelbergh, Robertus J. M. Klein Gebbink, Laura Filion, and Ingmar Swart, J. Phys. Chem. C, 120, (2016) : 318-323.
[30] Bartels, L. Tailoring Molecular Layers at Metal Surfaces. Nat. Chem., 2, 87−95, (2010).
[31] J. Kido, M. Kimura, and K. Nagai, Science 267, 1332, (1995)
[32] T. Malinski and Z. Tara, Nature London 358, 676 (1992) .
[33] Y. Harima, H. Okazaki, Y. Kunugi, K. Yamashita, H. Ishii, and K. Seki, Appl. Phys. Lett. 69, 1059 (1996)
[34] T. A. Heimer, C. A. Bignozzi, and G. J. Meyer, J. Phys. Chem. 97, 11987 (1993)
[35] A. Kühnle, Current Opinion in Colloid & Interface Science 14 (2009) 157–168.
[36] D. Nicholls (2014). Scanning tunneling microscopy and spectroscopy studies of zinc-phthalocyanne adsorption on SiC(0001) and iridium modified silicon surfaces: University of North Dakota.
[37] R. J. Hamers, *Annu. Rev. Phys. Chem*., 40, 531, (1989).
[38] H. Neddermeyer, *Rep. Prog. Phys*., 59, 701, (1996).
[39] F. Besenbacher, *Rep. Prog. Phys*., 59, 1737,(1996).
[40] C. Julian Chen, Introduction to Scanning Tunneling Microscopy, Oxford University Press, 1993.
[41] R. Wiesendanger, Scanning Probe Microscopy and Spectroscopy: Method and Applications, Cambridge University Press, 1994.)
[42] Bardeen, J. “Physical Review Letters.” *Physical Review Letters* 6.2 (1961): 57–59.
[43] Chen, C. J., 1993, Introduction to Scanning Tunneling Microscopy (Oxford University Press, New York).
[44] Feenstra, R. M., et al. “Tunneling Spectroscopy of the Si(111)2x1 Surface.” *Surface Science* 181.1-2 (1987): 295-306
[45] J. C. Vickerman, I. S. Gilmore, Surface analysis-the principal techniques, Wiley, 2009.
[46] K. Oura, V. G. LIfshits, A. A. Saranin, A. V. Zotov, M. Katayama, Surface Science: An Introduction, Springer, 2003.
[47] P. Hofmann, Lecture Notes on Surface Science, Arhus University, 2005.
[48] H. Hertz, *Annalen der Phyisk*, 33, 983,(1887).
[49] David S. Sholl, Janice A. Steckel, Density Functional Theory: A Practical Introduction, John Wiley & Sons, Inc., 2009.
[50] Y. P. Zhang, L. Yang, Y. H. Lai, G. Q. Xu, and X. S. Wang, Appl. Phys. Lett. 84, 401 (2004).

[51] H. Okino, I. Matsuda, R. Hobara, Y. Hosomura, S. Hasegawa, and P. A. Bennett, Appl. Phys. Lett. 86, 233108 (2005).
[52] A. Kida, H. Kajiyama, S. Heike, T. Hashizume, and K. Koike, Appl. Phys. Lett. 75, 540 (1999).
[53] R. Losio, K. N. Altmann and F. J. Himpsel, Phys. Rev. Lett. 85, 808 (2000).
[54] J. R. Ahn, H. W. Yeom, H. S. Yoon, and I. -W. Lyo, Phys. Rev. Lett. 91, 196403 (2003).
[55] D. Nicholls, N. Oncel, J. Phys. Condens. Matter 25, 445004 (2013).
[56] N. Oncel, D. Cakir, J. H. Dil, B. Slomski and G. Landolt, J. Phys. Condens. Matter 26, 285501 (2014).
[57] N. Oncel, A. van Houselt, J. Huijben, A. S. Hallback, O. Gurlu, H. J.W. Zandvliet, and B. Poelsema, Phys. Rev. Lett. 95, 116801 (2005).
[58] A. van Houselt, N. Oncel, B. Poelsema, and H. J.W. Zandvliet, Nanoletters 6, 1439 (2006).
[59] R. Losio, K. N. Altmann and F. J. Himpsel, Phys. Rev. Lett. 85, 808 (2000).
[60] J. L. McChesney, J. N. Crain, V. Perez-Dieste, F. Zheng, M. C. Gallagher, M. Bissen, C. Gundelach, and F. J. Himpsel, Phys. Rev. B 70, 195430 (2004).
[61] A. van Houselt, T. Gnielka, J. M.J. Aan de Brugh, N. Oncel, D. Kockmann, R. Heid, K. -P. Bohnen, B. Poelsema, and H. J.W. Zandvliet, Surf. Sci. 602, 1731 (2008).
[62] C. Blumenstein, J. Schäfer, S. Mietke, S. Meyer, A. Dollinger, M. Lochner, X. Y. Cui, L. Patthey, R. Matzdorf & R.Claessen, Nature Phys. 7, 776 (2011).
[63] J. H. G. Owen, K. Miki, and D. R. Bowler, J. Mater. Sci. 41**,** 4568 (2006).
[64] Y. Chen, D. A.A. Ohlberg, G. Mederios-Ribario, Y. A. Chang, and R. S. Williams, Appl. Phys. Lett. 76, 4004 (2000).
[65] Y. Chen, D. A.A. Ohlberg, and R. S. Williams, J. Appl. Phys. 91, 3213 (2002).
[66] J. Nogami, B. Z. Liu, M. V. Katkov, C. Ohbuchi, and N. O. Birge, Phys. Rev. B 63, 233305 (2001).
[67] O. Gurlu, O. A.O Adam, H. J.W. Zandvliet, and B. Poelsema, Appl. Phys. Lett. 83, 4610 (2003).
[68] J. Wang, M. Li, and E. I. Altman, Phys. Rev. B 70, 233312 (2004).
[69] T. F. Mocking, P. Bampous, N. Oncel, B. Poelsema, H. J. W. Zandvliet, Nature Commun. 4, 2387 (2013).
[70] N. Oncel, D. Nicholls, J. Phys. Cond. Matt., 25, 014010, 2013
[71] R. N. Mohottige, N. Oncel, Surf. Sci. 641, 237, 2015
[72] G. Kresse and J. Furthmuller, Comput. Mater. Sci. 6, 15 (1996) and G. Kresse and J. Furthmuller, Phys. Rev. B 54, 11169 (1996).
[73] P. E. Blochl, Phys. Rev. B, 1994, 50, 17953–17979 and G. Kresse and D. Joubert, Phys. Rev. B, 59, 1758–1775, (1999).
[74] H. J. Monkhorst and J. D. Pack, Phys. Rev. B, vol. 13, 5188, (1976).
[75] H. J.W. Zandvliet, Reviews of Modern Physics 72, 593, (2000).
[76] V. A. Ukraintsev, Z. Dohnalek, J. T. Yates, Jr. Surf. Sci. 388, 132, (1997).
[77] T. Yokoyama, K. Takayanagi, Phys. Rev. B, 61, R5078, (2000).
[78] A. C. Tickle, Thin-film Transistor: A New Approach to Microelectronics; Wiley, NY, 1999.
[79] A. A. A. Elshabini-Riad, F. D. Barlow, Thin-Film Technology Handbook, McGraw-Hill, NY, 1998.
[80] P.N. Dickerson, A. M. Hibberd, N. Oncel, S. L .Bernasek, Langmuir, 26, 18155, (2010).
[81] Y. Chin, D. Panduwinata, M. Sintic, T. J. Zum, N. S. Hush, M. J. Crossley and J. R. Reims, J. Phys. Chem. Lett. 2, 62, (2011).
[82] M. Hibino, A. Sumi, H. Tsuchiya, I. Hatta, J. Phys. Chem. B, 102, 4544, (1998).
[83] D. Nicholls, B. Ware, Z. Zhang, N. Oncel, Thin Solid Films, 534, 308, (2013).
[84] D. Nicholls, W. P. McKinzie, N. Oncel, J. Phys. Chem. C, 114, 14983, (2010).

[85] K. S. Mali, J. Adisoejoso, E. Ghijsens, I. De Cat, S. De Feyter, Acc. Chem. Res. 45, 1309, (2012).
[86] F. Tao, S. L. Bernasek, Langmuir, 23, 3513, (2007).
[87] K. Kim, K. E. Plass, A. J. Maztzger, J. Am. Chem. Soc. 127, 4879, (2005).
[88] P. Giannozzi, S. Baroni, N. Bonini, M. Calandra, R. Car, C. Cavazzoni, D. Ceresoli, G.L. Chiarotti, M. Cococcioni, I. Dabo, et al. J. Phys.: Condens. Matter 21, 395502, (2009).
[89] J. P. Perdew, K. Burke, M. Ernzerhof, Phys. Rev. Lett. 77, 3865−3868, (1996).
[90] F. Tao, J. Goswami, S. L. Bernasek, J. Phys. Chem. B. 110, 19562, (2006).
[91] P. N. Dickerson, A. M. Hibberd, N. Oncel, S. L. Bernasek, Langmuir, 26, 18155, (2010)
[92] Dubois E and Larrieu G Solid State Electron. 46 997, (2002).
[93] Larrieu G, Dubois E, Wallart X, Baie X and Katchi J, J. Appl. Phys. 94 7801, (2003).
[94] T. L. Lin, C. W. Nieh, S. Hashimoto, Q.F. Xiao, " Growth of IrSi3 by molecular beam epitaxy" *Thin Solid Films* 184, 343, (1990).
[95] D. A. Lange, G. A. Gibson, C. M. Falco, "Growth and structure of IrSi3 on Si(111)" *J. Appl. Phys.* 75, 2917, (1994).
[96] V. Demuth, H. P. Strunk, D. Worle, C. Kumpf, E. Burkel, M. Schulz, "Formation of amorphous layers by solid-state reaction. from thin Ir films on Si(100)" *Appl. Phys. A* 68, 451, (1999).
[97] Chu J J, Chen L J and Tu K N, J. Appl. Phys. 63, 1163, (1988).
[98] Almendra A, Rodriguez A, Rodriquez R, Shamin S N and Aksenova V I, J. Phys.: Condens. Matter 14, 3599, (2002).
[99] L. J. Chen, Mater. Sci. Eng. Rep. R29, 115 (2000).
[100] R. Benedictus, A. Bottger, E. J. Mittemeijer, Phys. Rev. B. 54, 9109 (1996).
[101] Peterson S, Baglin J, Hammer W, d'Heurle F, Kuan T S, Ohdomari I, de Soussa Pires J and Tove P, J. Appl. Phys. 50, 3357, (1979).
[102] Knapen W, Demeulemeester J, Deduysche D, Jordan-Sweet J L, Vantomme A, Van Meirhaeghe R L, Detavernier C and Lavoie C, Microelectron. Eng. 87, 258, (2010).
[103] Fatima, Oguz, I C, Cakir D, Hossain S, Mohottige R, Gulseren O, Oncel N, J. Appl. Phys., 095303, (2016).
[104] Hormann U, Thilo R, Klepeis J. E. , Pankratov O, Grunleitner H, Schulz M, Falke M and Bleloch A, Phys. Rev. B. 79, 104116, (2009).
[105] Nicholls D, Oncel N, J. Phys.: Condens. Matter 25, 445004, (2013).
[106] Oncel N, Cakir D, Dil J H, Slomski B and Landolt G, J. Phys.: Condens Matter, 26, 285501, (2014).
[107] H. Luth, "Solid Surfaces, Interfaces and Thin Films", Springer 3rd Ed., (2001).
[108] Waleed Azzam, Applied Surface Science 371, 562–570, (2016).
[109] Jean-Pierre Bucher, Lars Santesson,and Klaus Kern, Langmuir, Vol. 10, No. 4, (1994).
[110] Maud Jaouen, Céline Fiorini, Ludovic Douillard and Fabrice Charra, Nonlinear Optics and Quantum Optics, Vol. 46, pp. 299–308.
[111] D. Briggs and M. P. Seah. Practical surface analysis, Willey, New York (1983).
[112] Daniel Käfer, Gregor Witte, Piotr Cyganik, Andreas Terfort, and Christof Wöll, J. AM. CHEM. SOC., 128, 1723-1732, (2006).
[113] K. Xue, H. P. Ho, J. B. Xu, J. of Phys. D: Appl. Phys., 40, 2886-2893, (2007).
[114] Randy L. Vander Wal, Vicky M. Bryg, and Michael D. Hays, Anal. Chem., 83, 1924–1930, (2011).
[115] L. Dhanalakshmi, T. Udayabhaskararao and Thalappil Pradeep, Chem. Commun., 48, 859–861, (2012).

[116] R. Mohottige, S. Banerjee, N. Oncel "Coulomb blockade at room temperature: Self-assembled Iridium quantum dots on Si(110) surface", submitted.
[117] K. Konstadinidis, P. Zhang, R. L. Opila, D. L. Allara, Surf. Sci., 338, 300-312, (1995).
[118] Y. Ning, H. Xie, H. Xing, W. Deng and D. Yang, Surface and Interface Analysis, 24, 667-670, (1996).
[119] J. A. Gardella Jr., S. A. Ferguson, R. L. Chin, Appl. Spect. , 40, 224-232, (1986).